INL/JOU-20-59835-Revision-0

Improved natural convection heat transfer correlations for reactor cavity cooling systems of high-temperature gas-cooled reactors: From computational fluid dynamics to Pronghorn

Ramiro Freile, Mauricio Tano, Paolo Balestra, Sebastian Schunert, Mark Kimber

INL/JOU-20-59835-Revision-0

Improved natural convection heat transfer correlations for reactor cavity cooling systems of high-temperature gas-cooled reactors: From computational fluid dynamics to Pronghorn

Ramiro Freile, Mauricio Tano, Paolo Balestra, Sebastian Schunert, Mark Kimber

December 2021

Idaho National Laboratory
Idaho Falls, Idaho 83415

http://www.inl.gov

Prepared for the
U.S. Department of Energy
Under DOE Idaho Operations Office
Contract DE-AC07-05ID14517

Improved Natural Convection Heat Transfer Correlations for Reactor Cavity Cooling Systems of High-Temperature Gas-Cooled Reactors: From Computational Fluid Dynamics to Pronghorn

Ramiro Freile[1], Mauricio Tano[1], Paolo Balestra[2], Sebastian Schunert[2], Mark Kimber[1,3]
[1]Department of Nuclear Engineering, Texas A&M University
423 Spence St, College Station, TX 77843
[2] Idaho National Laboratory
775 MK Simpson Blvd, Idaho Falls, ID 83401
[3]Department of Mechanical Engineering, Texas A&M University
3127 TAMU, College Station, TX 77843

January 9, 2023

Abstract

The reactor cavity cooling system (RCCS) is a common reactor safety system in high-temperature gas-cooled Reactors (HTGR) that removes heat from the reactor pressure vessel (RPV) by radiation ($\sim 80\%$) and natural convection ($\sim 20\%$). For the simulation of accident scenarios of HTGRs, intermediate fidelity and system codes models must be employed to limit the models' execution time. While an accurate quantification of the radiative heat transfer is available in these models, the quantification of natural convection must rely on correlations of questionable accuracy for the Nusselt number. Commonly used correlations are based in experiments performed at low Rayleigh numbers and/or using isothermal walls in simplified geometries. This work improves on the accuracy of natural convection heat transfer correlations to support HTGR designs. These correlations include both local and average Nusselt numbers as a function of the global Rayleigh number, the local Rayleigh number, and the temperature profile at the hot wall of the RCCS. In the absence of dedicated experiments and the difficulty of performing high-fidelity simulations at realistic Rayleigh numbers, the data to fit the correlations are generated with computational fluid dynamics (CFD) using Reynolds Averaged Navier-Stokes (RANS) models. First, a careful selection of the RANS turbulence model is performed by comparing the results obtained with different RANS turbulence models against high-fidelity simulations of natural convection at Ra 1×10^{11} in a rectangular cavity. Next, the selected model is used to perform simulations of an HTGR cavity at different high Rayleigh numbers $\in [6.1 \times 10^{11}, 2.9 \times 10^{13}]$ to encompass several HTGR designs, assuming an isothermal RPV wall. The results obtained are used to fit a correlation for the average and space-varying Nusselt number as a function of the global and local Rayleigh numbers via a sparsity-promoting, least-squares method. The selected RANS model is then used to perform simulations of a PBMR-400 (Pebble Bed Modular Reactor) HTGR cavity with the temperature profiles at the RPV wall obtained during a PLOFC (Pressurized loss of forced cooling) transient. We use the results obtained to fit a temperature-dependent correction to the space-varying Nusselt number with the sparsity-promoting, least-squares method. The results obtained in

this work enable system-level codes, such as Pronghorn, to perform higher-fidelity simulations of the heat exchange process in the RCCS while still maintaining a low computational cost.

Keywords: Natural convection, Heat transfer correlations, High Rayleigh numbers, Reactor Cavity Cooling System, Pronghorn

1 Introduction

The high-temperature gas-cooled reactor (HTGR) is one of the Generation IV reactor concepts [1]. Owing to its resilience to high temperatures, this reactor design is able to ensure safety and reliability by allowing for a passive core heat removal from the uninsulated reactor vessel through the reactor cavity cooling system (RCCS) during accidents. In the event of a pressurized or depressurized loss of forced cooling (PLOFC or DLOFC), the RCCS represents the ultimate heat sink [2] [3]. Therefore, the RCCS design must ensure the integrity of the nuclear fuel, structures, and critical equipment by extracting the decay heat passively through natural convection or with the use of redundant forced convection cooling systems.

The RCCS design varies between different HTGR concepts [3, 4]. In some reactor concepts, such as the VGM [5], the high-temperature engineering test reactor (HTTR) [6], and the gas turbine modular gas reactor (GT-MHR) [7], the RCCS system consists of a large number of standpipes arranged in a circular pattern; the standpipes contain water that extracts the heat from the reactor cavity via forced convection. In other reactor designs, such as the high-temperature gas-cooled test reactor (HTR-10) [8] and the modular high-temperature gas-cooled reactor (MHTGR) [9], open chimneys are built on a side of the reactor hall to extract the heat via natural convection through thermal exchanges between the circulating air and the cavity. Nonetheless, in all cases, the key safety function of the system is extracting the decay heat from the reactor core via the reactor pressure vessel (RPV). Due to the high temperatures present in the RPV of HTGRs, the decay heat is transferred from the RPV wall to the RCCS predominantly via thermal radiation ($\sim$ 80%-90%) and, to a lesser extent, via natural convection ($\sim$ 10%-20%) [3]. Thermal radiation heat transfer in the RCCS can be accurately modeled using view factors [10]. However, modeling the natural convection heat exchange at the RPV wall is more challenging because of the high Rayleigh number turbulent phenomena in the RCCS. An accurate characterization of heat transfer between the RPV and the RCCS is of great importance for the design of HTGRs [11], especially in accident scenarios.

Taking into account natural convection in the RCCS is important for licensing and operating HTGRs. To demonstrate this, we created a simplified heat transfer model of a typical HTGR undergoing a pressurized loss of forced cooling transient with SCRAM. We assume that the instantaneous heat source drops to 7% of its nominal value and that the RCCS is at a fixed temperature of 350 K. The model is executed with and without the inclusion of natural convection heat transfer from the RPV wall. We find that the predicted RPV temperature increases by 40-50 K (500 vs. 550 °C) when neglecting natural convection heat transfer. To ensure sufficient margin to creep rupture, the maximum allowable temperature of the vessel during PLOFC transients is 538 °C [12]. As the predicted temperature with natural convection is below this threshold and the predicted temperature without natural convection is very close or even above this threshold, accurately accounting for natural convection in the RCCS is important.

Generally, experiments and high fidelity simulations are used to provide the correlations for the natural convection heat exchange coefficients. Nonetheless, on the experimental side, only scaled experiments of the RCCS cavity have been performed [13, 14]. These experiments focus on better understanding the secondary side of the RCCS system (i.e. flow conditions and heat transfer characteristics of the stand-pipes or chimneys). Furthermore, a full-scale experiment of the secondary side of an air-based RCCS has been built by Argonne National Laboratory [15]. The goal of this facility is to evaluate the performance of the

air-based RCCS design under a diverse set of conditions and to bound its performance. Nonetheless, none of these experiments is correctly scaled for studying the natural convection heat transfer in the RCCS. The experiments performed by Refs. [13, 14] are characterized by a much lower Rayleigh number than typical HTGR configurations. Thus, it is not expected that the heat exchange between the heated wall and the secondary side of the experiments accurately represents the natural convection heat exchange in HTGR-sized RCCS.

On the high-fidelity simulations side, to the authors' knowledge, the highest Rayleigh number achieved for natural convection flows with direct numerical simulation (DNS) is 1×10^{11} [16]. This Rayleigh number is roughly two orders of magnitude smaller than the one expected in the RCCS of power-reactor HTGR designs. The application of DNS to flows of these Rayleigh numbers is prohibitively expensive from the computational point of view. However, higher Rayleigh number CFD simulations of differentially heated rectangular cavities have been carried out using Reynolds Averaged Navier Stokes (RANS) models. Furthermore, these models have been successfully compared against experiments at lower Rayleigh number cavities (e.g., [17] [18]) and other CFD simulations [19] [20].

With the aim of accelerating the design and analysis cycle for HTGRs, Idaho National Laboratory (INL) has developed a coarse mesh thermal-hydraulic code named Pronghorn [21, 22]. Pronghorn is part of the ongoing effort within the multiphysics object oriented simulation environment (MOOSE) ecosystem [23] to develop fast core simulators using an intermediate fidelity approach. It avoids solving for lower-length scale phenomena, such as boundary layers, relying instead on closure correlations. To model the RCCS in Pronghorn, we must consider radiative and natural convection heat transfer. This work focuses on natural convection heat transfer. Thus, we require trustworthy natural convection heat transfer correlations in the full-scale RCCS system. Results of low-fidelity system codes in the literature employ simple correlations for the modeling of natural convective heat transfer [11]. However, these correlations are not adapted to the RCCS flow conditions and geometry. For example, these correlations are obtained for isothermal plates and only allow the computation of an averaged Nusselt number for the entirety of the plate. However, the RPV temperature of an HTGR during accident conditions is not isothermal. Temperature variations along the RPV have a significant impact on the local heat transfer characteristics expressed as the local Nusselt number. Hence, it is desirable to account for the differing Nusselt numbers along the RPV wall instead of using only an average value. Nonetheless, as previously discussed, the experiments and high-fidelity simulation data to develop a space-dependent correlation, including nonisothermal cases, are not available at the RCCS scale.

Therefore, considering the needs and limitations, this study uses RANS models implemented in the commercial code Star-CCM+ v14.04 to perform natural circulation simulations in realistic RCCS conditions (high Rayleigh numbers, $\sim 1 \times 10^{13}$). The resulting data is used to inform heat exchange correlations that take into account realistic RCCS conditions. RANS simulations allow for faster computations while still providing higher fidelity results than typical system codes, such as RELAP-5 [24], RELAP-7 [25], or SAM [26], or intermediate fidelity codes, such as Pronghorn or AGREE [27]. Hence, this paper contributes to solve the dichotomy of having accurate RCCS numerical models with a low computational cost. The developed correlations in this work include average and local Nusselt numbers, dependent upon the global and local Rayleigh numbers. Furthermore, the correlation is built for nonisothermal boundary conditions modeled after PLOFC conditions encountered in full-size HTGRs. The temperature variation along the RPV wall is important as it changes the local behavior of the heat transfer coefficient.

The remainder of this article is organized as follows:

- In Section 2, we present an assessment of the RANS turbulence models using Star-CCM+ against DNS for the heat transfer modeling of natural convection in rectangular cavities under high Rayleigh numbers regimes. This allows us to perform an informed selection of a RANS turbulence model that

best captures the heat transfer coefficient in conditions that are similar to the flow in an HTGR's RCCS cavity.

- In Section 3, we present the results of CFD simulations of a PBMR-400 RCCS geometry performed using the selected turbulence model. These simulations aim at (i) studying the dependency of the Nusselt number on the global and local Rayleigh number (Subsection 3.2) and (ii) analyzing the effect of nonisothermal boundary conditions on the Nusselt number profile (Subsection 3.3). The range of Rayleigh numbers used to tackle the first objective matches the range of expected Rayleigh numbers in different HTGR designs, ranging from an HTR-10 to a PBMR-400. The temperature profiles used as boundary conditions for the second goal are obtained by performing a simulation of a PLOFC accident using Pronghorn.

- In Section 4, using the data from Section 3, both the average and local Nusselt numbers along the RPV wall are fitted, considering its dependencies on the global Rayleigh number, the local Rayleigh number, and the wall temperature profile at the RPV. Correlations are developed in an incremental approach so that different correlations may be used according to the level of specificity required for the heat exchange coefficient.

2 Comparison between RANS models and DNS of a 1×10^{11} Rayleigh number differentially heated enclosure

The Rayleigh number in the RCCS of an HTGR is of the order of $1 \times 10^{12} - 5 \times 10^{13}$; for a given fluid (air) and small variations in the temperature difference, the Rayleigh number depends mostly on the height of the RCCS design. The large Rayleigh numbers arise from the fact that HTGRs typically feature tall and slender cores. The flow conditions under these Rayleigh numbers are highly turbulent. In the literature, the highest Rayleigh number achieved with DNS is 1×10^{11} for a differentially heated rectangular enclosure and was performed by [16]. The simulation of such a high Rayleigh number demands a high computational cost. In contrast, Reynolds Averaged Navier Stokes (RANS) models execute significantly faster than DNS, allowing parametric studies up to HTGR-RCCS Rayleigh number ranges. However, RANS models rely on modeling assumptions, such as the eddy viscosity model, and the selection of a suitable turbulence model. An assessment of the adequacy of the selected RANS model must be performed before deploying it for studying the problem of interest.

In order to assess the applicability of the RANS turbulence models, six different popular RANS models have been compared at $\mathrm{Ra} = 10^{11}$ against the DNS data [16] of a differentially heated rectangular enclosure of aspect ratio 4. The six RANS models used for comparison are Realizable k-ε (RKE) with Two-Layer Formulation, Elliptic Blending k-ε (EBKE), k-ω Shear Stress Transport (k-ω SST), Transition k-ω Shear Stress Transport (k-ω SST-γ), $v^2 f$, and Reynolds Stress Model with Two-Layer Formulation (RSM-two-layer). Specific details of each model are available in [28]. The simulations have been performed using the commercial software Star-CCM+ v14.04 [28]. The flow at large Rayleigh numbers is strongly turbulent and, therefore, unsteady. Therefore, the simulations are performed using an implicit, unsteady RANS model. The quantities of interest are obtained via averaging over a sufficiently long time period such that a statistically steady-state behavior is attained. The segregated solver is selected in Star-CCM+ to perform the simulations. This solver computes the energy, momentum, and continuity equations in an uncoupled manner, making use of the SIMPLE algorithm. A second-order upwind scheme is used for the advective terms and gradients are computed using the Green-Gauss cell-based method. For the density changes, the Boussinesq approximation

has been made. Regarding the flow parameters used, the Prandtl number is set to 0.71, and gravity is adjusted to obtain a Rayleigh number of $1x10^{11}$.

The geometry of the computational domain is identical to the domain used in [16]. A schematic representation of the geometry used in the DNS simulations is shown in Figure 1. Specifically, the dimensions for the height, width, and depth are set to 4, 1, and 0.5 m, respectively. Boundary conditions are assigned as follows: the vertical walls are set as isothermal walls, imposing a temperature difference of 1 K; the horizontal walls are adiabatic boundaries; and nonslip boundary conditions are applied to the four enclosing walls. The velocity and temperatures are assumed to be periodic in the direction perpendicular to the paper. The total number of elements used for the simulations are 8 million, 250 in the horizontal direction, 500 in the vertical direction, and 64 in the transverse direction. The maximum wall y^+ in the CFD simulations is 0.3. The final number of elements has been determined by testing further mesh refinements. Doubling the number of elements leads to a $\sim 1\%$ change in the position of the transition , a $\sim 0.2\%$ change in the maximum of the local Nusselt number and a $\sim 0.05\%$ of change in the global Nusselt number.

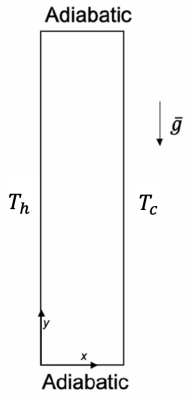

Figure 1: Sketch of the rectangular cavity domain used in [16].

The heat transfer coefficient is the main quantity of interest for an accurate prediction of the heat exchange in the RCCS. Figure 2 shows the comparison of the Nusselt number distribution along the hot wall between [16] and the results obtained with the RANS models. The x-axis of the graph in Figure 2 corresponds to the vertical coordinate in Figure 1 normalized by the cavity height.

Three regions can be distinguished in Figure 2, each with a unique heat transfer behavior along the hot wall: (1) a laminar-like region, (2) a transition region, and (3) a fully turbulent region. The behaviour of the heat exchange coefficient in these regions is closely related to the development of the flow as the fluid moves upwards along the cavity wall. In the first region, cold fluid traveling horizontally along the bottom adiabatic wall impinges on the lower part of the hot wall. The temperature gradient normal to the wall has a maximum in this region due to the abrupt difference of temperatures between the impinging cold fluid and the hot wall, explaining the heat transfer maxima at the leftmost of Figure 2. After the impingement, the fluid starts flowing in the upward direction with a laminar-like behavior, defining the profile obtained in region (1). So, the heat transfer coefficient decays along the hot wall. As the flow continues moving upwards, it is accelerated due to the effect of the buoyancy force, losing stability and presenting fluctuations characteristic of a turbulent transition. The point where these velocity fluctuations become important enough to dominate the flow profile in the boundary layer defines region (2), which presents a behaviour dominated by the transition to turbulence. In this region, the heat transfer increases due to the enhanced mixing that

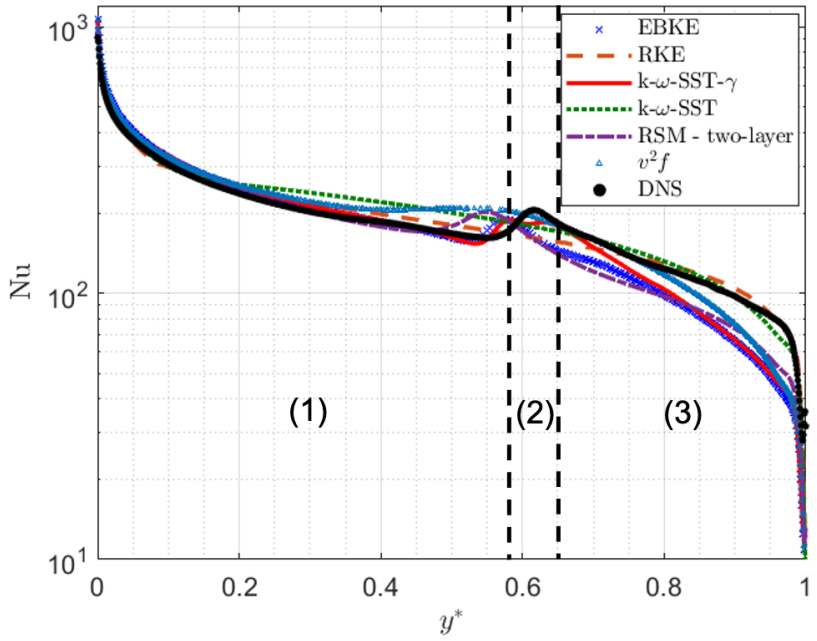

Figure 2: Nusselt number as a function of dimensionless height along the hot wall for the 6 RANS models and DNS.

accompanies velocity fluctuations. Region (3) begins after the transition point. Here, the flow becomes fully turbulent. The heat transfer coefficient decays towards the upper wall and experiences an extremely sharp decrease in close proximity to upper wall due to the stagnation point generated in the top-left corner of the domain. Similar to the flow approaching the hot wall at $y^* = 0$, the flow near the top at $y^* = 1$ impinges onto the upper adiabatic wall, causing a complex flow phenomenon. As demonstrated by DNS studies [16], vortices are shed in the normal and tangential direction to the top wall. The net effect of these complex flow physics is an adverse pressure gradient and flow deceleration in the top-left corner of the cavity.

The two equation models RKE and $k-\omega$ *SST* are originally calibrated to solve fully turbulent flows. Thus, they both approach the Nusslet number value in the turbulent region, but fail to reproduce the shape of the Nusselt number profile in the transition region and the laminar region as observed in Figure 2. The other four turbulence models introduce specific equations to capture the transition to turbulence. A description of the extra equations solved in each of these models, in addition to the turbulent kinetic energy and turbulent kinetic energy dissipation rate, are shown in Table 1. Therefore, we observe a better performance of these models in capturing the Nusselt number profile in Figure 2. Furthermore, Figure 2 also demonstrates that the transition to turbulence is best captured with the $k-\omega$ *SST* $-\gamma$ model because it captures both the transition location in the hot wall and the magnitude of the Nusselt number.

Figure 3 shows the local Nusselt number error as a function of the dimensionless height for all turbulence models. This allows for a comparison of the Nusselt number prediction by the different turbulence models in the three distinct regions, laminar, transition, and turbulent. By observing Figure 3, a representative division has been made for a qualitative comparison between models according to the flow conditions.

Table 1: Description of extra equations solved by the models.

RANS model	Description
EBKE & $v^2 f$	Equations for the elliptic blending functions to model the parabolic decay of the wall normal Reynolds stresses
$k-\omega\ SST-\gamma$	One extra equation for the intermittency parameter γ is solved. This parameter is an indicator of the flow regime in the boundary layer (i.e. if it's laminar, transitional or turbulent). It takes values between 0 (laminar) and 1 (turbulent). Then, the γ parameter modifies the production and dissipation of turbulent kinetic energy, accordingly. This model was originally added to the $k-\omega\ SST$ to enhance the modeling of the transition to turbulence.
RSM	Separate equations for each Reynolds Stress component plus a dissipation equation (RSM). Unlike the other models, the eddy viscosity approximation is not considered, allowing for the capturing of anisotropy in the flow.

Specifically, these regions are delimited using an *ad-hoc* qualitative criterion: $0.05 < y^* < 0.5$, $0.5 \leq y^* < 0.65$, $0.65 \leq y^* < 0.95$ for the laminar -region 1-, transition -region 2- and turbulent -region 3-, respectively. For quantification purposes, we make use of the L_1 relative error using the following expression:

$$L_{1\,rel} = \frac{1}{N^r} \sum_{i=1}^{N^r} \frac{||Nu_{RANS}(y_i^*) - Nu_{DNS}(y_i^*)||_1}{||Nu_{DNS}(y_i^*)||_1}, \tag{1}$$

where N^r is the total number of data points in the region r, which makes reference to laminar, transitional, and turbulent regions. Using the *ad-hoc* region division and the metric in Eq. 1, the models are compared with each other in each region. Table 2 displays the results of this comparison.

Table 2: L1 relative error norm of the Nusselt number in the three regions of interest between the six RANS models and DNS data.

	Laminar	Transition	Turbulent
EBKE	3.95%	2.76%	15.43%
RKE	6.01%	2.49%	3.72%
$k-\omega\ SST-\gamma$	4.65%	1.67%	9.96%
$k-\omega\ SST$	12.12%	3.47%	2.73%
RSM	3.81%	4.42%	15.12%
$v^2 f$	9.65%	3.56%	6.33%

The first conclusion from Table 2 is that RKE and $k-\omega\ SST$ models perform better than the rest in the turbulent region. Unlike their predecessors Standard $k-\varepsilon$ and $k-\omega$, these two models have an enhanced

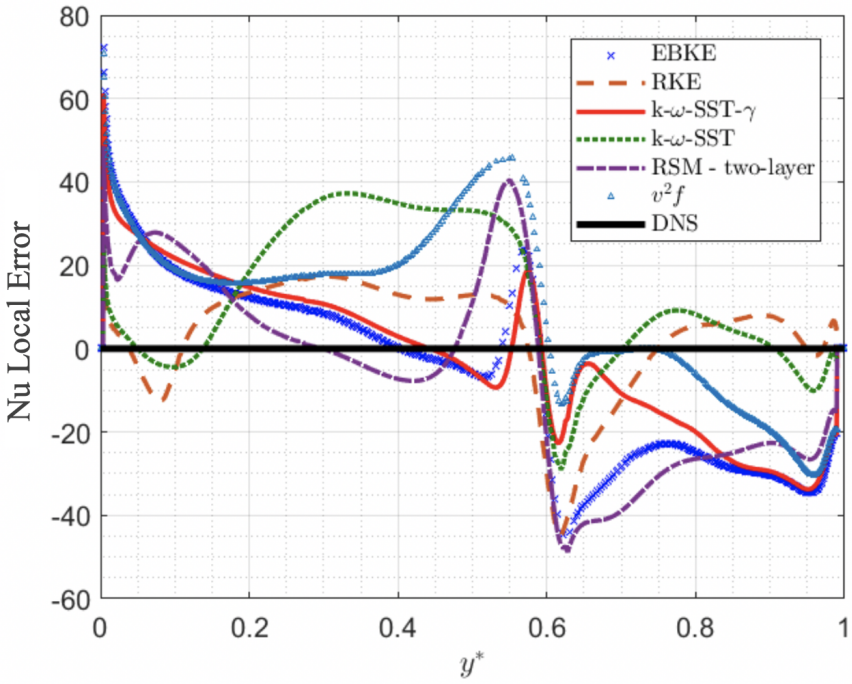

Figure 3: Nusselt number local error as a function of dimensionless height along the hot wall for the six RANS models and DNS.

capability of solving turbulent flows with adverse pressure gradients and flow separation. Nevertheless, they fail to reproduce the shape of the Nusselt number curve in the transition region adequately and over predict the Nusselt number in the laminar region.

Combining the capability of capturing the Nusselt number in the laminar and transitional region of the $k-\omega\ SST-\gamma$ model and the good predictions that the $k-\omega\ SST$ provides for the turbulent region leads to the conclusion that the $k-\omega\ SST-\gamma$ model has a great potential to outperform the rest of the models in the prediction of the heat transfer coefficient. It is worth noting that the $k-\omega\ SST-\gamma$ model predictions for the heat transfer coefficient should approach those of the $k-\omega\ SST$ in a fully turbulent flow. However, as seen in Figure 2, this is not the case. This is because, as previously observed, the upper wall introduces a complex flow phenomenon in the transition to turbulence. To verify this hypothesis, we perform a simulation increasing the Rayleigh number to 1×10^{12}, which approximates the Rayleigh number in an HTR-10 reactor. In this case, the transition region moves downwards and, hence, the effect of the upper wall in the transition region should be reduced. RANS simulations have been carried out using the $k-\omega\ SST-\gamma$ and $k-\omega\ SST$ models. Figure 4 shows the Nusselt number for both of the models. We observe that both models are in close agreement in the region after the turbulent transition and away from the upper wall.

As discussed earlier, the Rayleigh number in HTGRs is at least in the order of 1×10^{12}. Thus, it is expected that the transition occurs closer to the bottom wall than for the case studied in [16]. The simulations carried out in this section help us make an informed selection of the RANS model that best fits our purposes of simulating the natural convection in the RCCS, with the goal of providing heat transfer correlations to

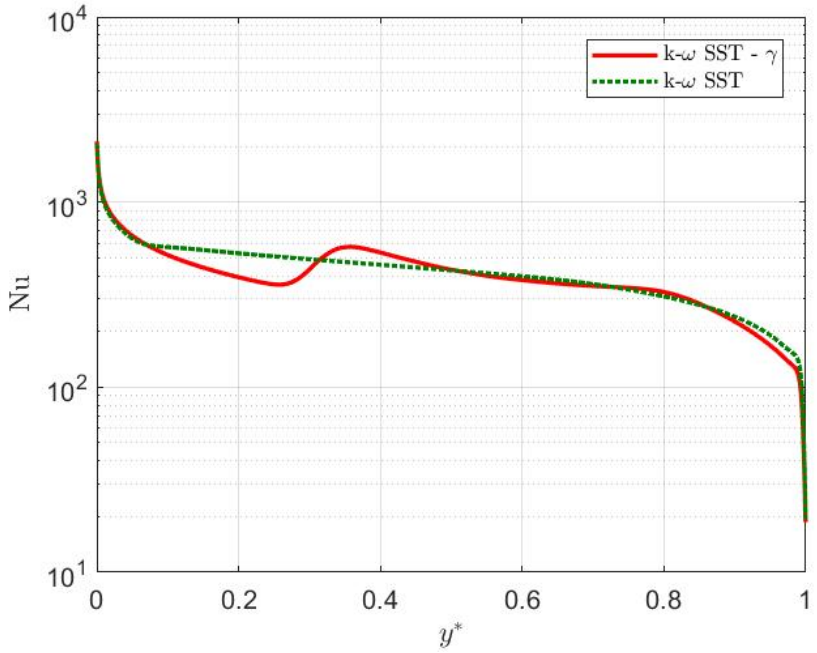

Figure 4: Nusselt number as a function of dimensionless height along the hot wall for the $k-\omega$ *SST* and $k-\omega$ *SST* $-\gamma$ models for Ra = 1×10^{12}.

coarse-mesh thermal hydraulics codes. All things considered, the $k-\omega$ *SST* $-\gamma$ is deemed adequate due to its enhanced capability of capturing: (i) the transition to the turbulence point, (ii) the value of the Nusselt number in the three regions, and (iii) the shape of the heat transfer in the three regions. In particular, this last item is important for our purposes of fitting a correlation for the local heat transfer coefficient along the hot wall of the RCCS.

3 Nusselt number dependencies on global and local Rayleigh number and on nonisothermal boundary conditions for an HTGR RCCS

This section is organized as follows:

First, we will study the dependence of the heat transfer coefficient distribution on the global and local Rayleigh number in a typical HTGR cavity configuration through CFD simulations. Second, we will study the dependence of the heat transfer coefficient distribution on the nonisothermal boundary conditions at the hot wall in a typical PBMR-400 cavity configuration through CFD simulations. Third, we will obtain Nusselt number values from the CFD simulations to inform the correlation fitting in the next section.

The Nusselt number dependency on the global Rayleigh number has been studied for a specific range of values that encompass different HTGR designs. The Nusselt number dependency on the nonisothermal boundary condition at the RPV hot wall has been studied by analyzing the heat transfer in a PBMR-400 cavity. The different temperature profiles imposed at the RPV in the CFD model correspond to different

stages in a PLOFC transient. The evolution of the temperature profile at the wall has been obtained by performing a simulation of a PLOFC transient in a PBMR-400 reactor using Pronghorn.

3.1 CFD RCCS cavity model

3.1.1 Computational domain

We model a realistic HTGR geometry after the PBRM-400 reactor benchmark [29]. The cavity of the PBMR-400 reactor is $\sim$ 22 m tall, and, as a result, the Rayleigh number of the cavity is very large ($\sim 5 \times 10^{13}$). The large Rayleigh number requires a large number of cells for the discretization of the domain. This makes the computational cost quite expensive, especially when repeated code evaluations are required (e.g., for a parameter sweep or the testing of different boundary conditions). To reduce the computational burden, a 2D axisymmetric section of the RCCS cavity is modeled in the simulations. The geometry of the 2D section model is presented in Figure 5. The x-axis is the axis of rotational symmetry for the axisymmetric model. The different parts of the model have been labeled with numbers from 1 to 5. These labels are:

1. RCCS cold wall with a height of 22.55 m and a distance of 4.62 m from the axis of rotation
2. Concrete top and bottom walls of the cavity
3. Top and bottom structures representing instrumentation (top) and supporting structures (bottom)
4. Hemi-ellipses representing the closure head-cap and bottom head-cap
5. RPV hot wall with a height of 17.7 m and a distance of 3.28 m to the axis of rotation.

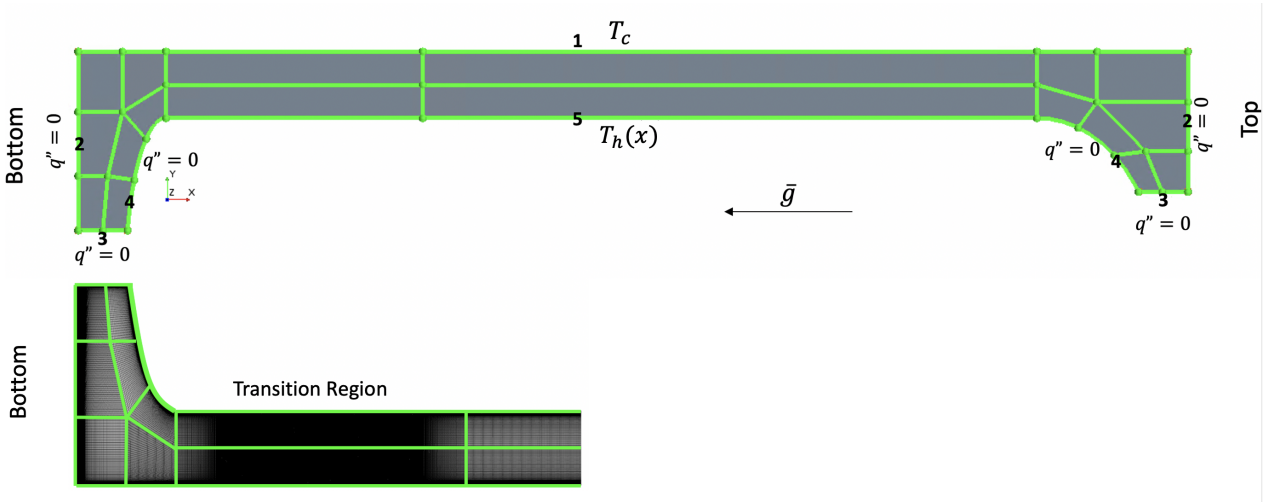

Figure 5: 2D axisymmetric model of the RCCS cavity.

The mesh is generated using the directed meshing tool in Star-CCM+, which uses a block meshing technique. The block divisions are shown in Figure 5. A mesh convergence study has been performed to determine the final mesh configuration. For this purpose, we computed heat transfer coefficients using

five different meshes with an increasing number of elements to test for grid independence. Four of the five meshes used for the study have been created by proportionally increasing the number of cells in the blocks, containing 0.5, 0.7, 1.4, and 2.8 million cells in total. During the mesh refinement study, it has been determined that the region where the transition occurs along the RPV requires a larger number of cells than other regions of the geometry to properly capture the shape of the heat transfer coefficient. As a result of this observation, the fifth mesh (referenced with the term hybrid mesh) places more elements in the transition region, as depicted in Figure 5, and contains 0.5 million cells in total. In addition, the mesh has been refined towards every wall of the domain to keep the dimensionless wall distance $y^+ < 1$. The element aspect ratio along the hot wall has been kept lower than 30. Figure 6 presents the heat transfer coefficient results for the five different meshes. The main conclusion of Figure 6 is that the hybrid mesh is able to obtain close to identical results in the turbulent and laminar region than the most refined mesh with 2.8 million cells. The relative difference in the location of the transition point between these two meshes is 1.5%. Using the locally refined mesh results is important for computational time saving, especially considering the fact that the envisaged parametric study requires multiple simulations.

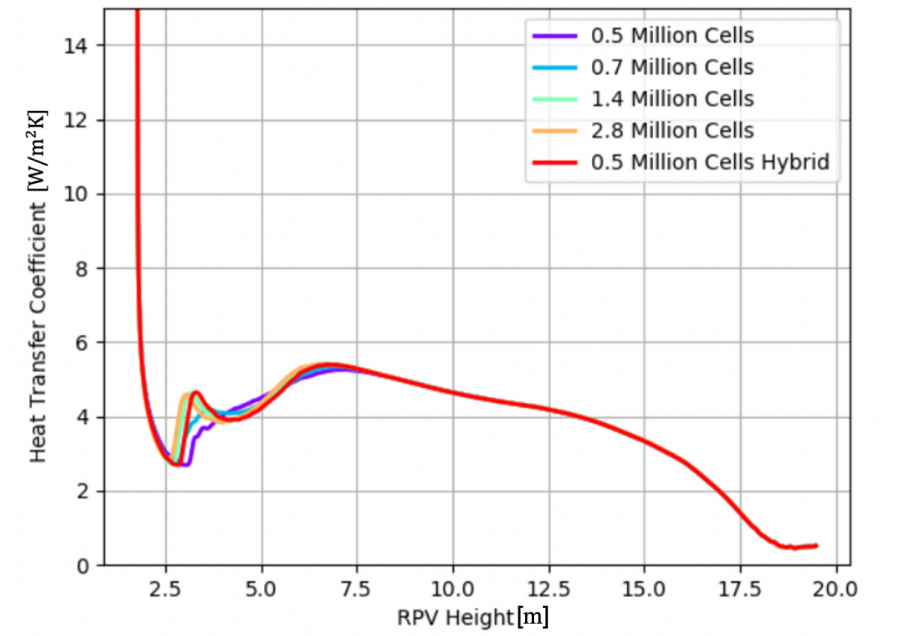

Figure 6: Heat transfer coefficient distribution on the hot wall for the refinement study considering five different meshes

3.1.2 Simulation parameters

The Reynolds Averaged Navier Stokes equations, Eq. A.2, are solved using the commercially available code Star-CCM+ v 14.04.011-R8. Star-CCM+ uses the finite volume method to discretize the RANS equations. The RANS model used is the $k-\omega$ $SST-\gamma$ (see Section 2). This model has been compared against DNS in similar conditions. Due to the large Rayleigh numbers of the studied cases, non-steady-state flows are expected, and, hence, a coupled implicit transient solver is used. The time step is chosen to keep the convective

Courant number close to unity. Even though this is not necessary for stability considerations in an implicit solver, a large time step might eventually affect the accuracy of the simulation and hinder convergence at every time step. The initial condition for the coupled solver is calculated by performing steady-state simulations with the segregated solver using the SIMPLE algorithm to perform pressure-velocity coupling. The initial guess for temperature and pressure fields in the steady-state simulations are set to 400 K and ambient pressure, respectively. The fields of interest such as velocity, temperature, and the heat transfer coefficient are obtained via averaging the unsteady flow field in the time-dependent simulations over a sufficiently long time period such that a statistically steady state is attained.

We discretize the advective terms in the momentum, turbulent kinetic energy, turbulent kinetic energy dissipation rate, and energy equation with the second-order upwind scheme [30]. The gradients are computed by using the Green-Gauss Cell-Based method, performing a weighted average of the values at the neighboring cell centers. The thermal conductivity and the kinematic viscosity of the air in the interior of the domain are given by Sutherland's law [31]. The density changes are taken into account using the ideal gas approximation. The specific heat of the air is set to 1010 $\frac{J}{kgK}$ due to the small variations expected in the temperature ranges studied. Gravity is fixed to $9.8\frac{\mathrm{m}}{\mathrm{s}^2}$ in subsection 3.3 and, in subsection 3.2, it is modified to impose the desired global Rayleigh numbers in the RCCS cavity.

Figure 5 depicts the boundary conditions used for the energy equation. For subsection 3.2, an isothermal boundary condition is used at the RPV wall, with a temperature value of 550 K. For subsection 3.3, a space-dependent temperature function is imposed at the RPV wall. The temperature profiles used in this subsection correspond to stages of a PLOFC transient modeled in Pronghorn. Details and results of this simulation are shown in subsection 3.3.1. Additionally, for the RCCS wall, a Dirichlet boundary condition is imposed with a value of 293.15 K. For simplification purposes, complex geometries, such as air risers, steel fins, and standpipes, have not been modeled. By using this boundary condition type, we are assuming that the RCCS secondary-loop pumping system assures the extraction of the decay heat and maintains a constant average temperature. Furthermore, during a PLOFC, hot air stagnates at the top of the reactor. For this reason, an isothermal boundary condition is set for the closure head-cap using the temperature value of the RPV at the junction (i.e., the upmost value of the temperature profile at the hot wall). In Section 3.2 this temperature is set to 450 K. Moreover, a no-slip condition is applied on all of the walls enclosing the cavity for the linear-momentum equation.

3.2 Nusselt number dependency on the global and local Rayleigh number for the isothermal boundary condition

The global Rayleigh number is defined as follows:

$$\mathrm{Ra} = \frac{g\beta\left(\overline{T_h} - T_c\right)L^3}{\nu\alpha}, \tag{2}$$

where g is the gravity, β is the thermal expansion coefficient calculated as $\frac{1}{T_m}$, where T_m is the mean temperature defined as $T_m = \frac{\overline{T_h}+T_c}{2}$. In addition, $\overline{T_h}$ is the average temperature at the RPV wall, and L is the height of the RPV wall. The thermal conductivity in α is evaluated at $\overline{T_h}$, while the rest of the thermophysical properties to calculate ν and α are evaluated at T_m.

The Rayleigh numbers considered for this subsection are in the range of 6.1×10^{11} to 2.9×10^{13}, which are representative of the expected dimensionless number in an HTR-10 ($L = 6.1$ m) and in a PBMR-400

($L \approx 17.7$ m), respectively. The local Nusselt number is defined as follows:

$$\mathrm{Nu}(x) = \frac{h(x)L}{k}, \quad h(x) = \frac{q"(x)}{(T_h(x) - T_c)}, \tag{3}$$

where $q"(x)$ is the local heat flux.

Figure 7 presents the results obtained for the Nusselt number distribution on the RPV wall for different Rayleigh numbers at an isothermal RPV wall temperature as a function of the dimensionless height $x^* = x/L$. As seen in Figure 7, the global Rayleigh number affects the magnitude of the average Nusselt number. This is because, as expected, the natural convective heat transfer increases with the buoyant source of momentum in the RCCS cavity. This is also to be expected because according to Eq. 2 the average RPV wall temperature increases when the Rayleigh number increases.

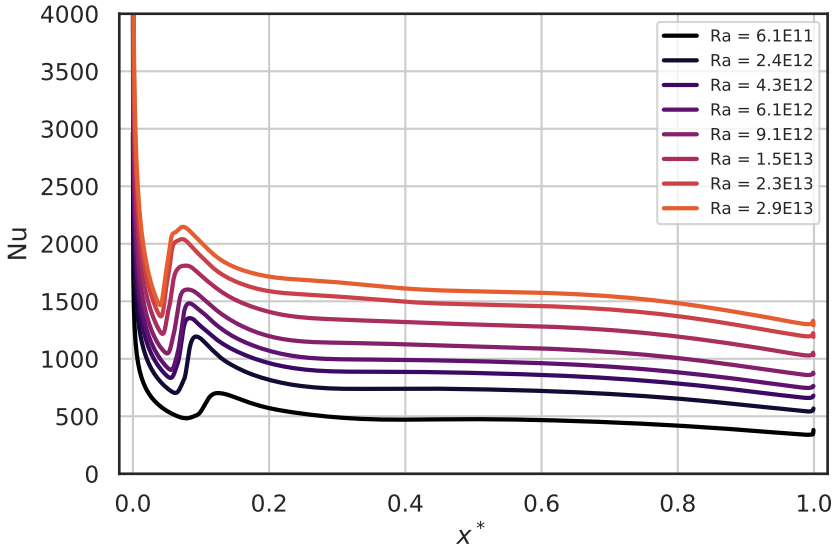

Figure 7: Nusselt number distribution on the RPV wall corresponding to isothermal boundary conditions at a Rayleigh number range.

In addition, the Nusselt numbers in Figure 7 follow a trend similar to the distribution in Figure 2. This behavior is related to the boundary layer development along the hot wall. The boundary layer develops and undergoes the transition to turbulence at a certain distance from the bottom part of the cavity. Along the different flow regimes (laminar, transition, and turbulent), the heat transfer coefficient has a different dependence to the local Rayleigh number. We define the local Rayleigh number as:

$$\mathrm{Ra}(x) = \mathrm{Ra}_x = \frac{g\beta\left(\overline{T_h} - T_c\right)x^3}{\nu\alpha}. \tag{4}$$

Finally, it is easy to note in Figure 7 that, considering the height of the problem fixed, the transition point moves towards the bottom of the RPV with the increase of the global Rayleigh number. Thus, we will need to capture the shifting in the transition region with the global Rayleigh number when fitting a correlation

for the Nusselt number. The studies for the nonisothermal boundary conditions are analyzed in the next subsection.

3.3 Nusselt number dependency on nonisothermal boundary conditions: PLOFC transient of a PBMR-400

3.3.1 Computing the RPV wall temperature profile: PBMR-400 Pronghorn/Rattlesnake PLOFC simulation

The PBMR-400 exercise is used for generating realistic RPV temperature profiles during a PLOFC transient. This transient is part of the PBMR-400 benchmark [29]. Transients in HTGRs are notoriously long—fifty hours for the benchmark's PLOFC and require the solution of the coupled neutron kinetic and thermal-hydraulics problem before the SCRAM. Full reactor core simulations of the entire transient are not performed using CFD tools because of the high computational cost. Instead, this type of simulation must rely on intermediate fidelity tools. In this study, the multidimensional thermal-hydraulics code Pronghorn [21] and the multidimensional radiation transport code Rattlesnake [32] are used for obtaining time-dependent temperature profiles along the RPV wall; both codes are based on MOOSE [23]. These codes are designed to solve the PLOFC fifty-hour transient in less than thirty minutes on a desktop computer. Details about the computational domain and simulation setup for the PLOFC transient are provided in Appendix B.

The temperature distributions along the RPV wall obtained throughout the PLOFC transient are depicted in Figure 8. Ten samples are taken every five hours of the PLOFC transient. During the transient, the peak temperature increases, and the location of the peak migrates upwards. This is expected during PLOFCs because the core remains pressurized and a significant amount of energy is transported from high-temperature regions in steady-state and regions with a large decay heat density upward towards the top of the core by natural circulation. The maximum temperature rises from about 600 K at the beginning of the transient to 675 K, while the peak temperature location migrates from 30% of the height of the active core region to about 60% of the height of the active core region. The ten temperature samples presented in Figure 8 are imposed as nonisotehrmal boundary conditions at the RPV wall for the CFD simulations. The results of these simulations are analyzed in the next section.

3.3.2 CFD simulations of the PBMR-400 RCCS cavity with nonisothermal boundary conditions at the RPV

3.3.2.1 Temperature and Velocity Fields

Unsteady RANS simulations using the $k-\omega\ SST-\gamma$ are performed imposing the ten temperature profiles in Figure 8 as the boundary condition for the RPV hot wall. As previously discussed in Subsection 3.3.1, it is important to note that these temperature profiles have been calculated in Pronghorn using a radiative heat transfer boundary condition added to a natural convection correlation. Even though radiation is not being modeled in the CFD simulations, imposing the Dirichlet boundary condition ensures that the buoyant force driving the flow corresponds to the actual temperature at the RPV wall. Nevertheless, previous studies [33] have demonstrated that, even with a Dirichlet boundary condition, radiation modeling can affect the natural convection in the cavity by modifying the temperature distribution on the horizontal adiabatic walls (concrete walls in our case). With this in mind, the radiation-convection interaction has been studied by comparing the effect of radiation on the convection heat transfer coefficient in a square cavity and a tall rectangular cavity with an aspect ratio of 10 (close to the one of the RCCS geometry). Results have shown that, although

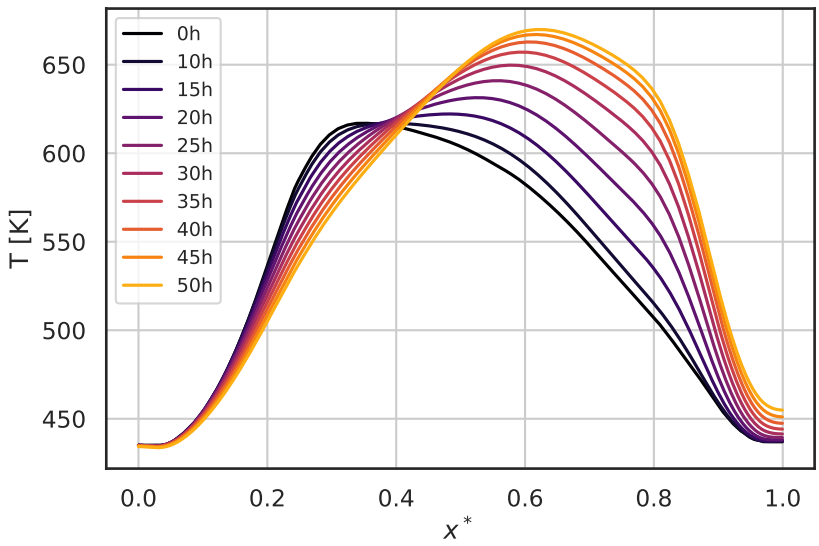

Figure 8: Temperature profiles along the RPV wall during a PLOFC at different stages of the transient as a function of the dimensionless height

radiation dampens the natural convection heat transfer in a square cavity, the influence of radiation on the convective heat transfer coefficient in the high aspect ratio cavity is negligible.

The time-averaged isotherms for the temperature profile twenty-five hours after the PLOFC are shown in Figure 9. The thermal boundary layer develops as it rises from the bottom of the RPV wall towards the top of the RCCS cavity. In the lower portion of the cavity, the opposed thermal boundary layers on the hot and cold wall do not interact with each other. Further downstream, it is observed that the thermal boundary layers merge. Figure 10 presents the streamlines in the cavity for the same temperature profile at the RPV wall. The lower part of the cavity remains motionless due to the negligible temperature gradient of the air (and consequent negligible buoyant force) in this region (Figure 9). The flow begins to develop on the bottom part of the RPV wall. As the flow develops, the fluctuations increase, up to the point where it undergoes the transition to turbulence. This transition zone is highlighted in the left part of Figure 10, where the streamlines are seen to adopt an irregular pattern. Past the transition zone, the flow becomes turbulent, the velocity boundary layer continues to develop along the RPV wall, and the flow attains the maximum velocity towards the top of the wall. At the top of the RPV, the flow expands and reverses its direction along the cold wall of the RCCS. As expected, the velocity profiles are not symmetric between the hot and cold wall due to the axisymmetry of the RCCS. Furthermore, the maximum magnitude of the velocity at the cold wall is lower than the hot wall, due to the area increment as a consequence of the larger radius. Figure 10 also shows that the upper central part of the cavity remains almost stagnant and that the velocity boundary layers do not interact considerably with each other.

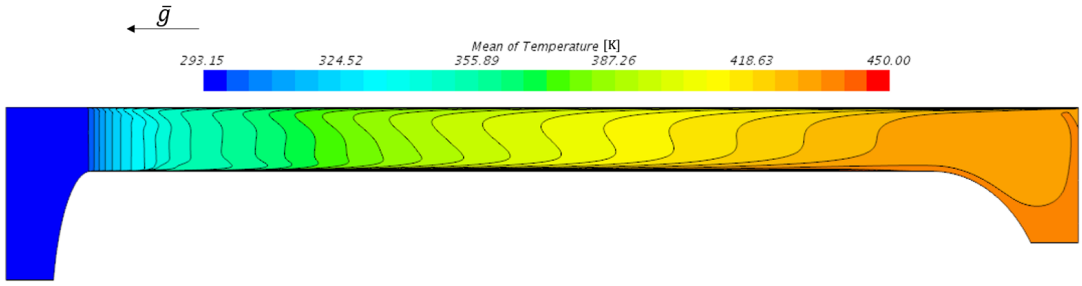

Figure 9: Contour plot of the isotherms in the RCCS cavity corresponding to the temperature boundary condition at t = 25h

.

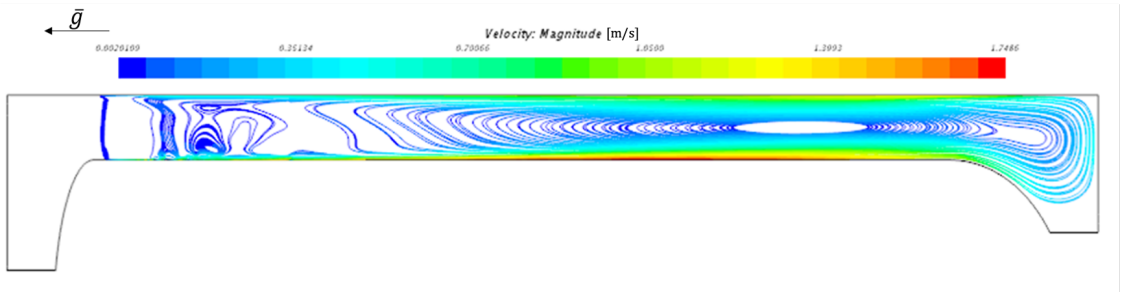

Figure 10: Velocity streamlines in the RCCS cavity corresponding to the temperature boundary condition at t = 25h

.

3.3.2.2 Heat Transfer

The Nusselt number distribution along the hot RPV wall for the 10 cases are presented in Figure 11. These Nusselt number distributions are similar to the results for the isothermal cases in Figure 7. The heat transfer decreases until the transition to turbulence occurs, where the Nusselt number increases locally. The main difference with the isothermal case is in the turbulent flow region. Analyzing both Figure 8 and Figure 11, it can be noted that the Nusselt number distribution along the hot wall follows the shape of the temperature profile at this wall. This observation is of particular interest for fitting the Nusselt number distribution with a dependency on the local wall temperature.

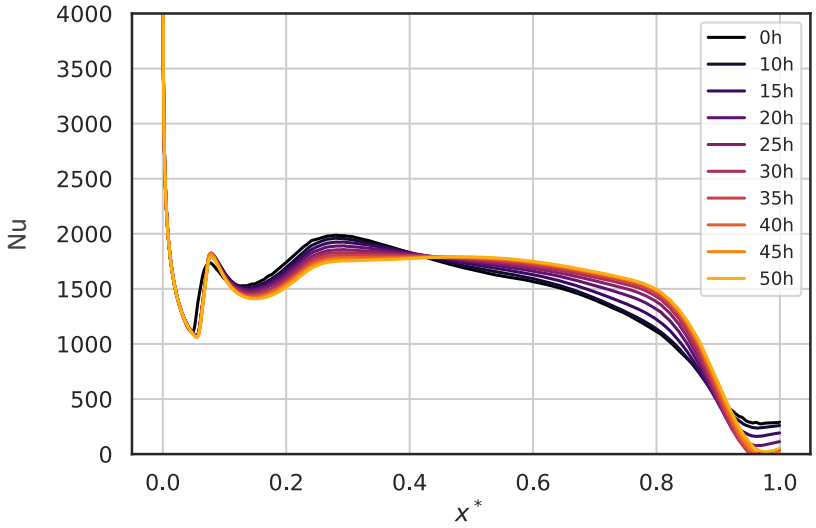

Figure 11: Nusselt number distribution on the RPV wall corresponding to the selected stages of the PLOFC transient

.

4 Fitting correlations for the heat exchange coefficients

In order for systems codes to take advantage of the insight gained from the CFD simulations, a correlation for the Nusselt profiles is needed. The development of these correlations is the focus of the present section. This section is divided into three parts. First, we explain the reasoning behind the fitting of the correlations. Then, we provide key details on the sparsity-promoting, least-squares technique used for fitting these correlations. Finally, we present and analyze the results obtained.

4.1 Procedure to fit a general correlation that is valid for isothermal and nonisothermal cases

The correlation developed should predict the Nusselt number at every point in the RPV wall. However, it should be robust in the sense that it should be applicable to diverse RCCS configurations, from the HTR-10 to the PBMR-400; Ra $\in [1 \times 10^{12}, 5 \times 10^{13}]$. Therefore, we will develop a correlation in a layered approach.

To illustrate the implementation of the layered approach, Figure 12 presents the temperature and Nusselt number profiles along the hot wall of the RPV for the beginning of the PLOFC transient. The red zone in the right frame of Figure 12 distinguishes the laminar, transition, and turbulent regions. It is first observed that the Nusselt number profile presents a significantly different behavior across each region. Therefore, for generalization purposes, each region should be treated separately when developing a robust correlation. Additionally, it is observed that the Nusselt number varies differently within the laminar, transition, and turbulent region. Hence, a different correlation should be fitted in each region. Finally, an important corre-

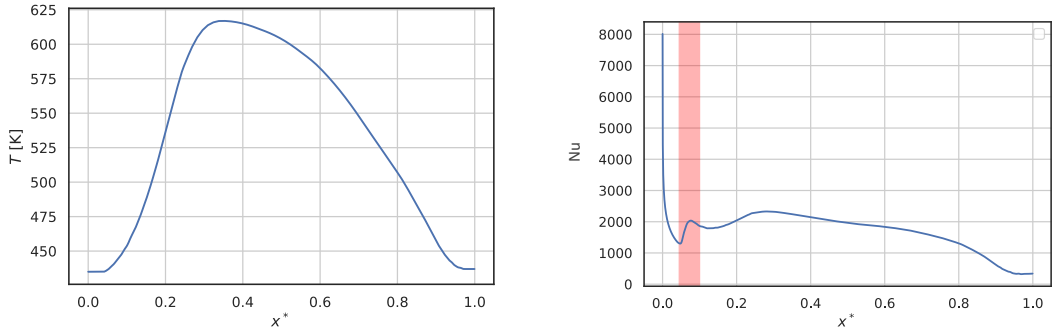

Figure 12: Temperature (left) and Nusselt number (right) over the vertical wall of the RPV at the beginning of the PLOFC transient.

lation between the Nusselt number and the wall temperature profile is observed; we must account for this correlation in the nonisothermal case.

In short, we will first fit a correlation to distinguish the laminar, transition, and turbulent regions. Once the regions have been identified, we will fit two correlations. The first one will be for the average Nusselt number in each of the regions. The second one will be for the discrepancy between the local and the average Nusselt number. This second correlation will allow us to describe the space dependency of the Nusselt number along the RPV wall. For these two cases, we will use the isothermal studies performed in Subsection 3.2. This is because the larger range of Rayleigh numbers in these studies will provide a larger validity envelope to the fitted correlations. Using the nonisothermal cases studied in Subsection 3.3, we will fit a correlation for the thermal discrepancy in the Nusselt number profile caused by the nonisothermal temperature boundary condition. The validity range of this thermal correction is smaller. The reason of this layered approach is to provide engineers and researchers with useful correlations that they can use when modeling the RCCS system. In this sense, the correlation developed for the average Nusselt number per zone already provides an improvement to studies using a constant Nusselt number correlation. If larger accuracy is required, the engineer can choose to implement the space-dependent correction. These two correlations are valid across the range of Ra numbers expected for different RCCS systems. Finally, for the particular case of an RCCS of the PBMR-400, thermal corrections due to nonisothermal boundary conditions may be implemented. The procedure and reasoning behind fitting each of these correlations are explained in the following paragraphs.

First, we must fit a correlation identifying the start and end of the turbulent transition. Based on similar studies of the turbulent transition in natural convection in enclosures [34, 35], the global Rayleigh number should determine the beginning and end of the turbulent-transition. Thus, we will solve for functions as follows:

$$x^*_{\mathrm{s,tr}} = f_{\mathrm{s,tr}}(\mathrm{Ra}), \quad x^*_{\mathrm{e,tr}} = f_{\mathrm{e,tr}}(\mathrm{Ra}), \tag{5}$$

where $x^*_{\mathrm{s,tr}}$ and $x^*_{\mathrm{e,tr}}$ are the nondimensional distances for the start and end of the transition, respectively, and $f_{\mathrm{s,tr}}$ and $f_{\mathrm{e,tr}}$ are fitting functions that will be determined during the fitting process.

The beginning and end of the transition $x^*_{\mathrm{s,tr}}$ and $x^*_{\mathrm{e,tr}}$ are then used to split the Nusselt number profiles presented in Figure 7 in three regions: laminar, transition, and turbulent. Then, for each of these regions, a correlation for the average Nusselt number is fitted. According to previous studies [16, 35] and the nondimensional laws for mass, momentum, and energy [16] the average Nusselt number in each of these regions

should be a function of the global Rayleigh number as follows:

$$\begin{cases} \overline{\mathrm{Nu}}_l = \overline{f}_l(\mathrm{Ra}) \quad \text{for} \quad x^* \in [0, x^*_{\mathrm{s,tr}}], \\ \overline{\mathrm{Nu}}_{tr} = \overline{f}_{tr}(\mathrm{Ra}) \quad \text{for} \quad x^* \in [x^*_{\mathrm{s,tr}}, x^*_{\mathrm{e,tr}}], \\ \overline{\mathrm{Nu}}_{tu} = \overline{f}_{tu}(\mathrm{Ra}) \quad \text{for} \quad x^* \in [x^*_{\mathrm{e,tr}}, 1], \end{cases} \tag{6}$$

where $\overline{\mathrm{Nu}}_l$, $\overline{\mathrm{Nu}}_{tr}$, $\overline{\mathrm{Nu}}_{tu}$ are the average Nusselt number for the laminar, transition, and turbulent regions, respectively, and $\overline{f}_l$, $\overline{f}_{tr}$, and $\overline{f}_{tu}$ are fitting functions to be determined over this range. Using the average Nusselt number in each region, the average Nusselt number over the whole domain can be determined as follows:

$$\overline{\mathrm{Nu}} = x^*_{\mathrm{s,tr}}\overline{\mathrm{Nu}}_l + (x^*_{\mathrm{e,tr}} - x^*_{\mathrm{s,tr}})\overline{\mathrm{Nu}}_{tr} + (1 - x^*_{\mathrm{e,tr}})\overline{\mathrm{Nu}}_{tu}\,. \tag{7}$$

Note, however, that due to large variations in the Nusselt number profile across the RPV wall, large local errors will still be obtained, even with the region-separated Nusselt correlation developed in Eq. 6. A discrepancy function between the Nusselt number obtained by CFD and the average one for the laminar, transition, and turbulent regions is fitted to improve the local description of the Nusselt number. For each of the three regions, we define the discrepancy function dependent on the nondimensional height x^* as follows:

$$\begin{cases} d_l(x^*) = \mathrm{Nu}(x^*) - \overline{\mathrm{Nu}}_l \quad \text{for} \quad x^* \in [0, x^*_{\mathrm{s,tr}}], \\ d_{tr}(x^*) = \mathrm{Nu}(x^*) - \overline{\mathrm{Nu}}_{tr} \quad \text{for} \quad x^* \in [x^*_{\mathrm{s,tr}}, x^*_{\mathrm{e,tr}}], \\ d_{tu}(x^*) = \mathrm{Nu}(x^*) - \overline{\mathrm{Nu}}_{tu} \quad \text{for} \quad x^* \in [x^*_{\mathrm{e,tr}}, 1], \end{cases} \tag{8}$$

where $d_s(x^*)$, $d_{tr}(x^*)$, and $d_{tu}(x^*)$ are the laminar, transition, and turbulent discrepancy functions defined as the difference between the actual Nusselt profile and the average one fitted in Eq. 6. According to the nondimensional laws describing the buoyant flow in an enclosure [16], this discrepancy can only be a function of the global Rayleigh number (Eq. 2) and the local Rayleigh number defined in Eq. 4. Therefore, our fitting hypothesis reads as follows:

$$\begin{cases} d_l(x^*) = f_{\mathrm{d,l}}(\mathrm{Ra}, \mathrm{Ra}_x) \quad \text{for} \quad x^* \in [0, x^*_{\mathrm{s,tr}}], \\ d_{tr}(x^*) = f_{\mathrm{d,tr}}(\mathrm{Ra}, \mathrm{Ra}_x) \quad \text{for} \quad x^* \in [x^*_{\mathrm{s,tr}}, x^*_{\mathrm{e,tr}}], \\ d_{tu}(x^*) = f_{\mathrm{d,tu}}(\mathrm{Ra}, \mathrm{Ra}_x) \quad \text{for} \quad x^* \in [x^*_{\mathrm{e,tr}}, 1], \end{cases} \tag{9}$$

where $f_{\mathrm{d,l}}$, $f_{\mathrm{d,tr}}$, and $f_{\mathrm{d,tu}}$ are the fitting functions for the laminar, transition, and turbulent discrepancy, respectively. Hence, the global space-dependent Nusselt number profile can be described as follows:

$$\begin{aligned} \mathrm{Nu}(x^*) = \left(\overline{\mathrm{Nu}}_l + d_l(x^*)\right)\left(\mathscr{H}(0) - \mathscr{H}(x^*_{\mathrm{s,tr}})\right) + \left(\overline{\mathrm{Nu}}_{tr} + d_{tr}(x^*)\right)\left(\mathscr{H}(x^*_{\mathrm{e,tr}}) - \mathscr{H}(x^*_{\mathrm{s,tr}})\right) + \\ \left(\overline{\mathrm{Nu}}_{tu} + d_{tu}(x^*)\right)\left(\mathscr{H}(x^*_{\mathrm{e,tr}}) - \mathscr{H}(1)\right), \end{aligned} \tag{10}$$

where $\mathscr{H}$ is the Heaviside function.

At this point, the correlations developed should be valid for the RCCS enclosure with an isothermal boundary condition in the range of Rayleigh numbers $\mathrm{Ra} \in [6.1 \times 10^{11}, 2.9 \times 10^{13}]$ used in the CFD studies. However, as observed by comparing Figures 8 and 11, there is a significant correlation between the Nusselt number and temperature profiles over the RPV wall for the nonisothermal case. Therefore, a temperature correction must be added to the correlation. At first, thermal corrections with the argument dependency $T(x^*) - \overline{T}$ were evaluated, where $\overline{T}$ is the average temperature over the RPV wall. However, this argument dependency led to poor fitting performance due its change of signs. Hence, correlations with the argument dependency $\frac{T(x^*)}{\overline{T}}$ are preferred. The thermal discrepancy function is then defined in a multiplicative form, trying to preserve the correlations developed in the isothermal case for the nonisothermal one. As it has been

done previously, a different temperature correction will be fitted for the laminar, transition, and turbulent regions, which are expressed as follows:

$$\begin{cases} d_{\text{th,l}}(x^*) = \frac{\text{Nu}(T(x^*),x^*)}{\overline{\text{Nu}}_l d_l(x^*)} = f_{\text{th,l}}(\frac{T(x^*)}{\overline{T}}) \quad \text{for} \quad x^* \in [0, x^*_{\text{s,tr}}], \\ d_{\text{th,tr}}(x^*) = \frac{\text{Nu}(T(x^*),x^*)}{\overline{\text{Nu}}_{tr} d_{tr}(x^*)} = f_{\text{th,tr}}(\frac{T(x^*)}{\overline{T}}) \quad \text{for} \quad x^* \in [x^*_{\text{s,tr}}, x^*_{\text{e,tr}}], \\ d_{\text{th,tu}}(x^*) = \frac{\text{Nu}(T(x^*),x^*)}{\overline{\text{Nu}}_{tu} d_{tu}(x^*)} = f_{\text{th,tu}}(\frac{T(x^*)}{\overline{T}}) \quad \text{for} \quad x^* \in [x^*_{\text{e,tr}}, 1], \end{cases} \tag{11}$$

where $f_{\text{th,l}}$, $f_{\text{th,tr}}$, and $f_{\text{th,tu}}$ are the fitting functions for the multiplicative thermal discrepancies for the laminar, transition, and turbulent regions, respectively. Note also that, for the isothermal case, we have $T(x^*) = \overline{T}$ for all x^* at the RPV wall. Hence, the nonisothermal correction will not modify the isothermal correlation. The final expression for the space-dependent Nusselt number with thermal correction reads as follows:

$$\begin{aligned} \text{Nu}(x^*) = \left(\overline{\text{Nu}}_l + d_l(x^*)\right) d_{\text{th,l}}(x^*) \left(\mathscr{H}(0) - \mathscr{H}(x^*_{\text{s,tr}})\right) + \left(\overline{\text{Nu}}_{tr} + d_{tr}(x^*)\right) d_{\text{th,tr}}(x^*) \left(\mathscr{H}(x^*_{\text{e,tr}}) - \mathscr{H}(x^*_{\text{s,tr}})\right) + \\ \left(\overline{\text{Nu}}_{tu} + d_{tu}(x^*)\right) d_{\text{th,tu}}(x^*) \left(\mathscr{H}(x^*_{\text{e,tr}}) - \mathscr{H}(1)\right). \end{aligned} \tag{12}$$

Up to this point, we have identified the arguments of the fitting functions $f_{\text{s,tr}}$, $f_{\text{e,tr}}$, $\overline{f}_l$, $\overline{f}_{tr}$, $\overline{f}_{tu}$, $f_{\text{d,l}}$, $f_{\text{d,tr}}$, $f_{\text{d,tu}}$, $f_{\text{th,l}}$, $f_{\text{th,tr}}$, and $f_{\text{th,tu}}$. Before fitting these functions to the data, we must propose a functional form for each of these functions. We will follow a data-driven approach for this purpose using a sparsity-promoting, least-squares technique. We provide details about this method in the following section.

4.2 Sparsity-promoting, least-squares method for fitting correlations

The sparsity-promoting, least-squares techniques used in this work is based on the methods developed in [36, 37]. Some key details about these methods are provided in this section.

The data-set consists of 5000 equispaced samples of the Nusselt number at points on the RPV wall in the x^*-direction for each Rayleigh number studied. As described in Subsection 4.1, each data-set is divided into laminar, transition, and turbulent regions. For the isothermal case, the Nusselt profiles are computed in Subsection 3.2 and the results are presented in Figure 7 for eight different Rayleigh numbers between $[6.1 \times 10^{11}, 2.9 \times 10^{13}]$. The data-array consists of the flattened array of Nusselt number samples ordered from smallest to largest Rayleigh number as follows:

$$\mathbf{Nu}_{iso,n} = \begin{bmatrix} \text{Nu}(x^*_1, \text{Ra} = 6.1 \times 10^{11}) \\ \vdots \\ \text{Nu}(x^*_{N_n}, \text{Ra} = 6.1 \times 10^{11}) \\ \vdots \\ \vdots \\ \text{Nu}(x^*_1, \text{Ra} = 2.9 \times 10^{13}) \\ \vdots \\ \text{Nu}(x^*_{N_n}, \text{Ra} = 2.9 \times 10^{13}) \end{bmatrix}, \tag{13}$$

where n represents the region (laminar, transition, or turbulence) and N_n are the number of points in this region. Bootstrapping by cubic-splines in the lower-sampled Rayleigh numbers is implemented so that each

region contains the same number of samples as the largest-sampled one for all Rayleigh number. This procedure is important to uniformize biases across the Rayleigh range.

A similar array is built for the nonisothermal case presented in Subsection 3.3 but using the results obtained from the ten samples during the PLOFC transient with $t \in [0, 50]$ hours. The following flattened array is obtained:

$$\mathbf{Nu}_{noniso,n} = \begin{bmatrix} \mathrm{Nu}(x_1^*, t = 0\mathrm{h}) \\ \vdots \\ \mathrm{Nu}(x_{N_n}^*, t = 0\mathrm{h}) \\ \vdots \\ \vdots \\ \mathrm{Nu}(x_1^*, t = 50\mathrm{h}) \\ \vdots \\ \mathrm{Nu}(x_{N_n}^*, t = 50\mathrm{h}) \end{bmatrix}. \tag{14}$$

Note that each data-array is then adapted to each fitting case. For instance, the average Nusselt number in each region for each Rayleigh number will be introduced in each component of the data-array for that Rayleigh number when fitting a correlation for the average Nusselt number at each region. Additionally, the discrepancy between the Nusselt number in Eq. 13 and the average Nusselt number for each Rayleigh number will be used when fitting the isothermal discrepancy function per each region. The discrepancy between Eq. 14 and the Nusselt number predicted from the isothermal fitting (average value plus discrepancy) will be used to fit the temperature discrepancy. Finally, the computed beginning and end of the turbulent transition will be added as data-points for each Rayleigh number when fitting the correlations for the beginning and end of this transition, respectively. Slightly abusing notation, we will generically name the data $\mathbf{Nu}_f$, where f represents the fitting case.

We will require the fitting functions to approximate each data-set point-by-point. For this purpose, it is convenient to construct flattened arrays to evaluate the arguments of the fitting functions at each x^*-position where a sample point is taken and for each Rayleigh number. For example, the global Rayleigh number dependency array for the isothermal case may be defined as follows:

$$\mathbf{Ra}_{iso,n} = \begin{bmatrix} \mathrm{Ra} = 6.1 \times 10^{11}\big|_1 \\ \vdots \\ \mathrm{Ra} = 6.1 \times 10^{11}\big|_{N_n} \\ \vdots \\ \vdots \\ \mathrm{Ra} = 2.9 \times 10^{13}\big|_1 \\ \vdots \\ \mathrm{Ra} = 2.9 \times 10^{13}\big|_{N_n} \end{bmatrix} \tag{15}$$

and the one for local Rayleigh number as follows:

$$\mathbf{Ra}_{\mathbf{x}iso,n} = \begin{bmatrix} 6.1\times10^{11}(x_1^*)^3 \\ \vdots \\ 6.1\times10^{11}(x_{N_n}^*)^3 \\ \vdots \\ \vdots \\ 2.9\times10^{13}(x_1^*)^3 \\ \vdots \\ 2.9\times10^{13}(x_{N_n}^*)^3 \end{bmatrix}. \tag{16}$$

Equivalent arrays can be constructed for the nonisothermal case. Additionally, to account for the temperature dependency in the nonisothermal case, an array $\overline{\mathbf{T}}$ is constructed by sampling the temperature and its average value at each of the x^* positions defined in the data-set for each Rayleigh number.

The following step is to build a database of potential fitting functions with the arguments identified in subsection 4.1. To illustrate this method, as example of the unary function, let us take fitting the average Nusselt number in the laminar region as a function of the global Rayleigh number, $\overline{f}_l(\mathrm{Ra})$. The goal is to generate a large set of random functions and then let a sparsity-promoting, least-squares method define the function or functions that best fit the data-set. To generate the large set of random functions, we will introduce a set of unary operators, $\mathscr{O}_1 = \{\hat{\cdot}, \exp, \sin, \cos, \Gamma\}$, that are power, exponentiation, sine, cosine, and the Γ-function, respectively, and a set of binary operators, $\mathscr{O}_2 = \{+, -, *, /\}$, that are addition, subtraction, multiplication, and division, respectively. The argument, the global Ra number in this example case, is randomly combined with the functions in the operator set to produce a set of random test functions to be included in the database. Exogenous fitting coefficients are added to the fitting functions if needed. In the example of $\overline{f}_l(\mathrm{Ra})$, one may envision random functions, such as $a\mathrm{Ra}^b$, $a\exp(b\mathrm{Ra})$, $a(\exp(a\mathrm{Ra}) + \mathrm{Ra}^c)$, where a is an internal free-parameter that can be fitted with a least-squares approach and b and c ~~is an~~*are* external free-parameter*s* that must be fitted with an exogenous optimization routine. For the case of binary fitting functions, such as the discrepancy in the laminar region $f_{\mathrm{d,l}}(\mathrm{Ra}, \mathrm{Ra}_x)$, the procedure is similar, except that both arguments are randomly combined to produce the fitting functions. In the example of the discrepancy in the laminar region, one may find functions such as $a\mathrm{Ra}^b\mathrm{Ra}_x^c$ or $a(\mathrm{Ra}^b + \mathrm{Ra}_x^c)$.

Each of the randomly generated fitting functions is now evaluated in the flattened argument-arrays, and the results are stacked column-by-column in a candidates matrix. This reads as follows:

$$\theta_f = \begin{bmatrix} | & | & \cdots & | \\ f_1(\mathbf{Ra}, \mathbf{Ra}_x, \overline{\mathbf{T}}; \mathbf{p}_{ex}) & f_2(\mathbf{Ra}, \mathbf{Ra}_x, \overline{\mathbf{T}}; \mathbf{p}_{ex}) & \cdots & f_M(\mathbf{Ra}, \mathbf{Ra}_x, \overline{\mathbf{T}}; \mathbf{p}_{ex}) \\ | & | & \cdots & | \end{bmatrix}, \tag{17}$$

where θ_f is the candidate matrix for one of the fitting functions f identified in Subsection 4.1, f_i is one of the randomly generated candidates for the fitting function, and $\mathbf{p}_{ex}$ is a vector of exogenous parameters defining the random candidate. Note that the argument dependency $(\mathbf{Ra}, \mathbf{Ra}_x, \overline{\mathbf{T}})$ has been included for generality; although only one or two of these arguments will be used for each case, as identified in Subsection 4.1 for each fitting function. A total of $M = 10^5$ random functions are generated for each fitting case in this study.

Next, using the candidate matrix, a prediction for the data-set can be generated as follows:

$$\mathbf{Nu}_f^{pred} = \theta_f(\mathbf{Ra}, \mathbf{Ra}_x, \overline{\mathbf{T}}; \mathbf{p}_{ex})\mathbf{c}, \tag{18}$$

where $\mathbf{c} \in \mathbb{R}^M$ is a coefficient of vectors determined by solving the sparsity-promoting, least-square problem. In our method, the solution of this problem seeks to minimize the L_2-norm between the predicted and measured data, introducing an L_1 Lasso-penalty to promote sparsity in the fitting coefficient. The optimization problem reads as follows:

$$\mathbf{c} = \underset{\mathbf{c}',\mathbf{p}_{ex}}{\operatorname{argmin}} \|\mathbf{Nu}_f - \theta_f(\mathbf{Ra}, \mathbf{Ra}_x, \overline{\mathbf{T}}; \mathbf{p}_{ex})\mathbf{c}'\|_2^2 + \lambda_1 \|\mathbf{c}'\|_1 \,, \tag{19}$$

where λ_1 is the Lasso-regression penalty set to $\lambda_1 = 0.1$ in each optimization problem to obtain compact expressions that can be more easily implemented in system-level codes. The solution of the optimization problem is performed in two stages. First, the optimal values for the exogenous parameters $\mathbf{p}_{ex}$ are computed with an unconstrained Levenberg-Marquardt optimization algorithm [38]. This yields the best possible expression for each function in the candidate matrix. Next, the constrained optimization problem for $\mathbf{c}$ is taken to its dual-form, leading to a conic-programming problem, and the resulting problem is solved with a Newton optimization algorithm [39].

The advantage of this approach is that we approximately avoid preassuming a functional form to fit arguments to data by generating a large number of random candidate functions and then selecting the best-fit candidate or candidates. Hence, contrary to similar works in the literature, we avoid introducing prior biases in assuming a functional form that can limit the model performance. The results obtained with this optimization method are discussed in the following subsection.

4.3 Results for the fitting correlations

Correlations for the beginning and end of the turbulent transition are fitted for the isothermal case. For the beginning of the turbulent transition, the best functional form for the fitting correlation determined by the sparsity-promoting, least-squares regression is $x^*_{\mathrm{s,tr}} = e^{a\,\mathrm{Ra}^b}$. The fitting of the correlation yielded $a = -0.4777$ and $b = 0.06165$. A similar functional form was identified for the end of the turbulent transition $x^*_{\mathrm{e,tr}} = e^{a\,\mathrm{Ra}^b}$, and the fitting yielded $a = -0.4349$ and $b = 0.05607$. The results obtained are presented in Figure 13. In general, a good fitting performance is observed. The mean-squared fitting errors are 2% for the beginning of the transition and 8% for the end of the transition. Since the end of the turbulent transition is determined via a second-order method as the point where the curvature in the Nusselt number profile changes sign (indicating a fully developed turbulent regime), a larger noise and, hence, fitting error is obtained. Nonetheless, these errors yield little importance when fitting correlations for the Nusselt number, since the results of the correlations and not the data-points are used when splitting the data-set in laminar, transition, and turbulent regions. For completeness, the fitted correlations for the beginning and end of the turbulent transition are:

$$\begin{aligned} x^*_{\mathrm{s,tr}} &= e^{-0.4777\,\mathrm{Ra}^{0.06165}} \\ x^*_{\mathrm{e,tr}} &= e^{-0.4349\,\mathrm{Ra}^{0.05607}} \end{aligned} \tag{20}$$

Next, the average Nusselt number for the isothermal cases as a function of the global Rayleigh number is fitted. The average Nusselt number correlations found by the sparsity-promoting, least-squares method are the following:

$$\begin{cases} \overline{\mathrm{Nu}}_l = 0.2490\,\mathrm{Ra}^{0.2911} & \text{for} \quad x^* \in [0, x^*_{\mathrm{s,tr}}]\,, \\ \overline{\mathrm{Nu}}_{tr} = 0.1901\,\mathrm{Ra}^{0.2994} & \text{for} \quad x^* \in [x^*_{\mathrm{s,tr}}, x^*_{\mathrm{e,tr}}]\,, \\ \overline{\mathrm{Nu}}_{tu} = 0.08169\,\mathrm{Ra}^{0.3183} & \text{for} \quad x^* \in [x^*_{\mathrm{e,tr}}, 1]\,. \end{cases} \tag{21}$$

The results obtained for the fitting of the Nusselt number in each region as a function of the Rayleigh number are presented in the left top frame of Figure 14. In general, a good fitting is observed with the correlations

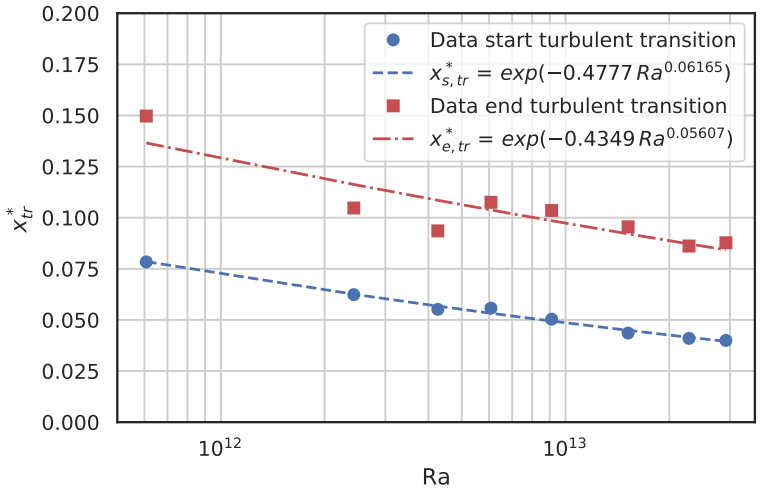

Figure 13: Comparison of data-points and correlation fitting for the end of the turbulent transition.

developed in Eq. 21. In fact, the mean-squared errors for fitting the laminar, transition, and turbulent regions over the Rayleigh number range are 0.4%, 2.6%, and 0.1%, respectively. Note that these errors are smaller than the fidelity that can be expected from a CFD code.

Using the results of Eq. 20 and Eq. 21, an average Nusselt number over the whole domain can be defined according to Eq. 7. The actual Nusselt number profile is compared against the Nusselt number correlation by region and a global correlation for the average Nusselt number for the example case of $\mathrm{Ra} = 1.5 \times 10^{13}$ in the bottom frame of Figure 14. Even though the Nusselt number by parts performs well in capturing the mean Nusselt number, a worse performance is observed when capturing the local Nusselt number. The mean-squared error in capturing the local Nusselt number for all Rayleigh numbers is 14% when using a Nusselt number by parts and 17% when using an average Nusselt number, while the maximum error can be larger than 300%. Therefore, we see the need of fitting a discrepancy function to correct this behaviour.

The results for the fitted discrepancy functions are the following:

$$\begin{cases} d_l(x^*) = 4166.5 - 4496.1\ \mathrm{Ra}^{-0.01444}\ \mathrm{Ra}_x^{0.03856} & \text{for} \quad x^* \in [0, x^*_{\mathrm{s,tr}}], \\ d_{tr}(x^*) = 215.8 - 0.9437\ \mathrm{Ra}^{0.7742}\ \mathrm{Ra}_x^{-1.3474} & \text{for} \quad x^* \in [x^*_{\mathrm{s,tr}}, x^*_{\mathrm{e,tr}}], \\ d_{tu}(x^*) = -1952.8 - 1455.9\ \mathrm{Ra}^{0.02974}\ \mathrm{Ra}_x^{-0.03135} & \text{for} \quad x^* \in [x^*_{\mathrm{e,tr}}, 1], \end{cases} \tag{22}$$

The results obtained for the Nusselt number profile by adding the discrepancy function to the Nusselt number fitted by parts are presented in Figure 15 for three different Rayleigh numbers. It is observed that adding the discrepancy function provides a significant improvement in the space description of the Nusselt number profile. Larger errors are still obtained close to the beginning and end of the transition regions, but, in general~~ly~~, a significantly improved fitting-performance is observed across the laminar and turbulent regions. The mean fitting error for all Rayleigh numbers is reduced to 4% and the maximum error is reduced to 9% when adding the discrepancy. Note that the discrepancy function is valid across the Rayleigh number range used in the isothermal simulations.

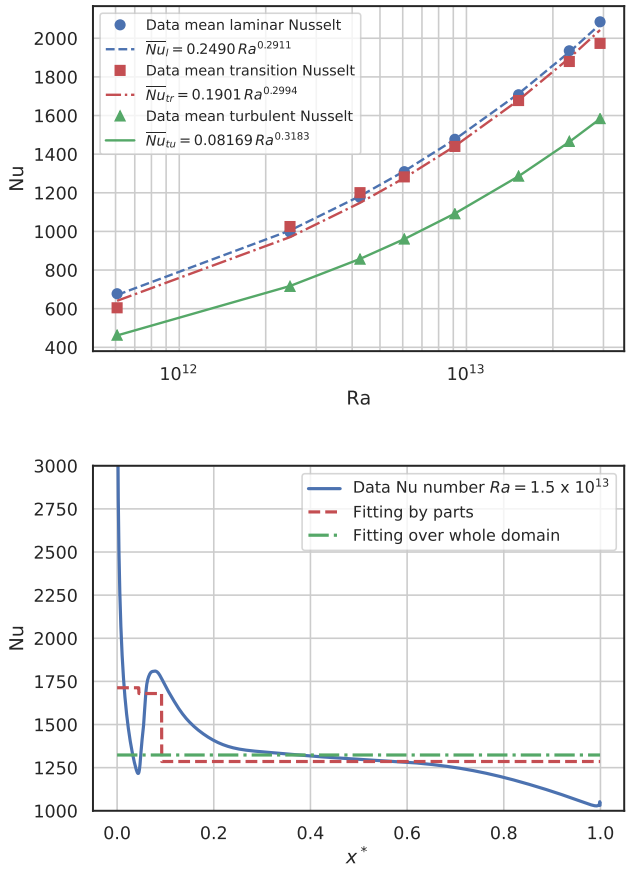

Figure 14: Top: comparison between the data and fitted average Nusselt number in the laminar, transition, and turbulent regions as a function of the Rayleigh number. Bottom: comparison between the data-computed Nusselt profile, the Nusselt number fitted by parts, and the Nusselt number fitted over the whole domain for the case with $\mathrm{Ra} = 1.5 \times 10^{13}$.

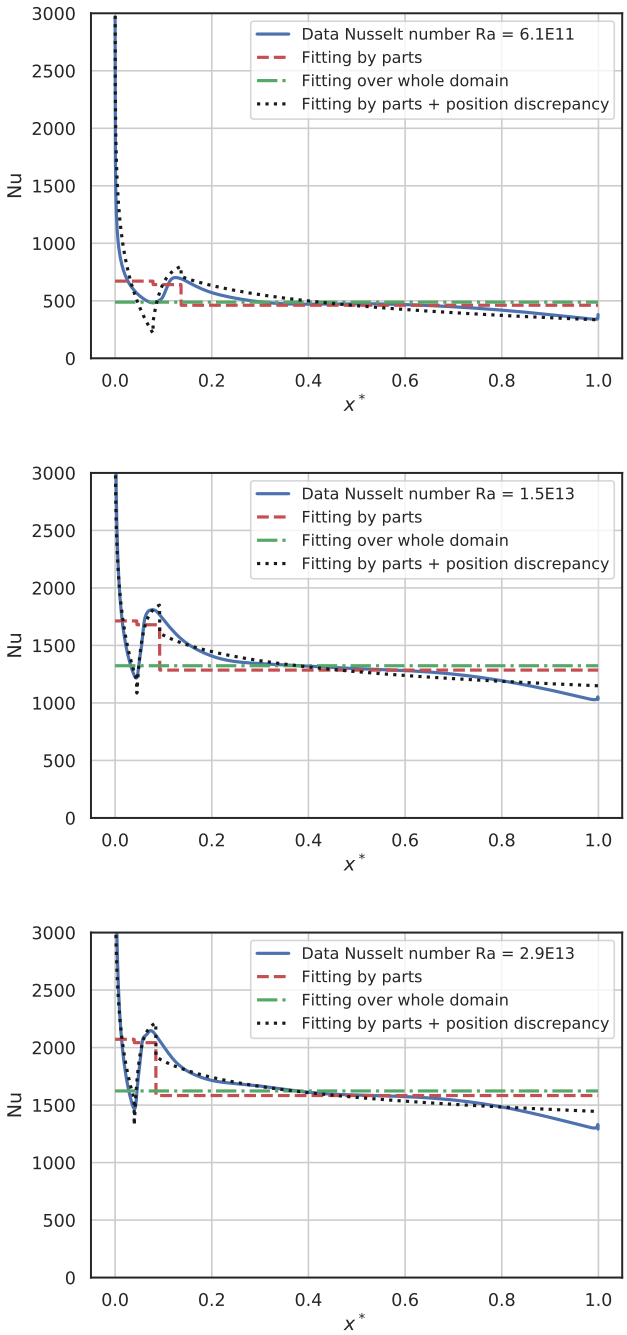

Figure 15: Comparison of the actual Nusselt profile with the average Nusselt number over the whole domain, the Nusselt number by parts, and the Nusselt number by parts corrected with the discrepancy for (top) $\mathrm{Ra} = 6.1 \times 10^{11}$, (center) $\mathrm{Ra} = 1.5 \times 10^{13}$, and (bottom) $\mathrm{Ra} = 2.9 \times 10^{13}$.

Finally, the temperature-based corrections for the nonisothermal case must be fitted. The results obtained for these discrepancy functions are the following:

$$\begin{cases} d_{\mathrm{th,l}}(x^*) = 0.8742 \left(\frac{T(x^*)}{\overline{T}}\right)^{-1.1122\times10^{-}6} & \text{for} \quad x^* \in [0, x^*_{\mathrm{s,tr}}], \\ d_{\mathrm{th,tr}}(x^*) = 0.7580 \left(\frac{T(x^*)}{\overline{T}}\right)^{-1.1102\times10^{-}6} & \text{for} \quad x^* \in [x^*_{\mathrm{s,tr}}, x^*_{\mathrm{e,tr}}], \\ d_{\mathrm{th,tu}}(x^*) = 1.4214 - 0.3924 \left(\frac{T(x^*)}{\overline{T}}\right)^{-4.7124} & \text{for} \quad x^* \in [x^*_{\mathrm{e,tr}}, 1], \end{cases} \tag{23}$$

Note that, inevitably, the thermal corrections introduce a bias in the ones developed for the isothermal case. This is logical since the nonlinear convective acceleration in the development of a heated boundary layer over a heated wall will be affected nonlinearly by the heating distribution, hence modifying the average Rayleigh numbers. Furthermore, we note that the corrections over the laminar and transition region can roughly be predicted by scaling the isothermal Nusselt profile with a constant term. Nonetheless, a more marked space-dependency appears in the turbulent region, where the Nusselt profile more closely follows the temperature one. Due to this particular correction behaviour introduced by the nonisothermal heating, we can only recommend the use of these temperature corrections for PLOFC transients in the PBMR-400 RCCS. The effects of adding the thermal discrepancies in correcting the Nusselt number profile are presented in Figure 16. It is observed that the thermal corrections significantly improve the description of the Nusselt profile. In fact, the average error for the ten samples across the transient is 20% without using the thermal correction but 4% when including it.

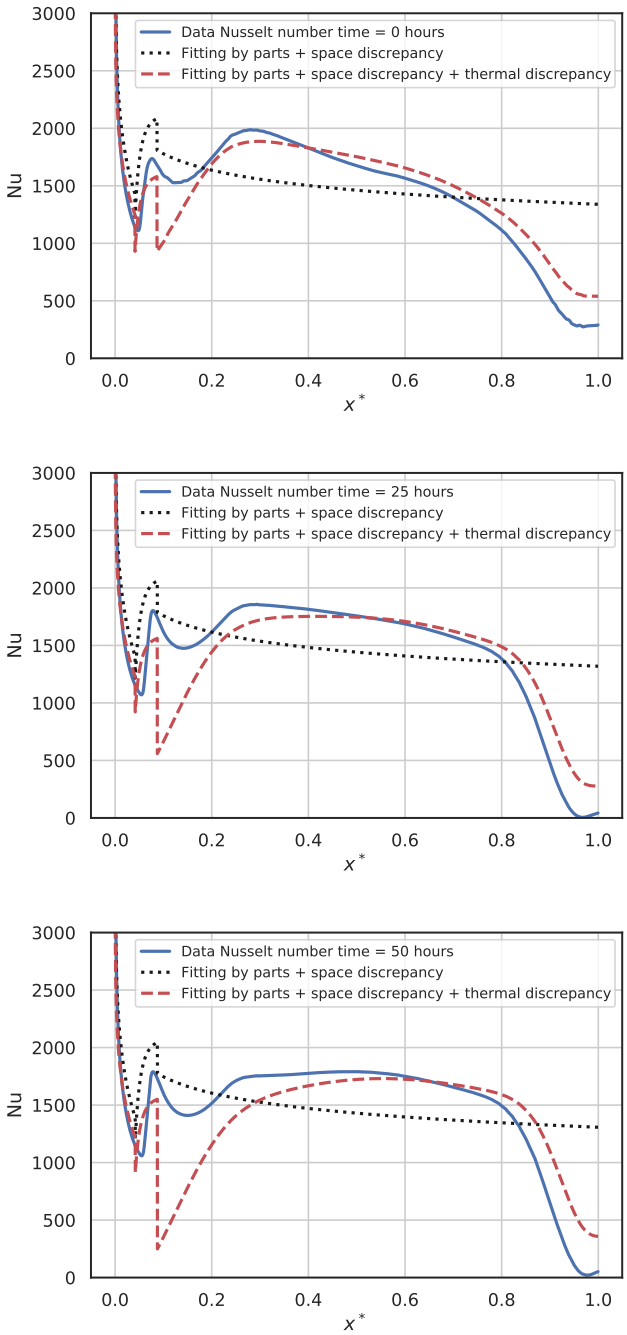

Figure 16: Comparison of the actual Nusselt profile with the Nusselt number by parts corrected with the space discrepancy, with and without thermal discrepancies for (top) 0 hours, (center) 25 hours, and (bottom) 50 hours after a PLOFC transient.

5 Conclusions

This paper provides natural convection heat transfer correlations tailored for modeling the heat loss on the RPV surface in LOFC conditions to the RCCS that are valid for Rayleigh numbers ranging from 6.1×10^{11} to 2.9×10^{13}, which roughly span the size from HTR-10 to PBMR-400. Current correlations only model the average Nusselt number with isothermal temperature profiles. However, the CFD simulations performed in this paper have demonstrated that the flow conditions next to the RPV wall and the nonuniform temperature profiles at this wall produce significant local variations in the Nusselt number. Hence, using the average Nusselt number correlations in isothermal conditions yield high local errors when studying localized convective heat transfer.

Addressing this problem, the natural convection heat transfer correlations developed in this paper provide an improvement to existing ones by (i) allowing for the computation of local heat transfer conditions via a local Nusselt number and (ii) by accounting for the influence of nonuniform temperature distributions along the RPV wall on the local Nusselt number using a realistic HTGR RCCS geometry. Capturing the local Nusselt number is important because the natural convective heat transfer coefficient (and Nusselt number) changes its behavior along the RPV wall according to the flow conditions. Also, it is critical to capture the influence of the local temperature values at the RPV wall, as it also affects the mean value and behavior of the local Nusselt number. This last item is particularly relevant during a LOFC transient, where the temperature distribution, being far from isothermal, undergoes significant changes both in values and in shape.

The provided correlations are intended for use in system codes, such as RELAP-5 or SAM, or intermediate fidelity codes, such as Pronghorn or AGREE. For the RCCS cavity, these codes are designed to rapidly perform transient simulations making detailed CFD calculations computationally infeasible. However, these codes must capture the relevant physical phenomena in the RCCS for providing accurate estimates of the temperature evolution during relevant transient scenarios.

In this paper, the data obtained from CFD RANS codes inform the development of correlations for the average and local Nusselt number in HTGR RCCS cavities. First, the $k-\omega\ SST-\gamma$ RANS model has been selected among six RANS-models candidates by comparing the results of the heat transfer coefficient to the DNS data in [16]. The CFD simulations of the RCCS cavity use this selected model. The fitting of the correlations from the CFD data has been accomplished using the sparsity-promoting, least-squares method that determines not only the fitting coefficients but also the most appropriate function for these correlations. The isothermal correlations are valid for a range of Rayleigh numbers $\mathrm{Ra} \in [6.1 \times 10^{11}, 2.9 \times 10^{13}]$, which encompasses different HTGR designs, from the HTR-10 to the PBMR-400. Besides, the dependency on nonisothermal boundary conditions at the hot wall has also been considered for a PBMR-400, using temperature profiles obtained in a PLOFC simulation using Pronghorn. The average difference of the fitting and CFD results for the isothermal cases is 4%, and the maximum local difference is 9%. For the nonisothermal temperature boundary conditions, the average difference for the ten temperature cases is 4%. In summary, the correlations obtained in this work allow coarse-mesh thermal-hydraulic codes, such as Pronghorn, to mimic the natural convection heat transfer exchange in an HTGR RCCS of higher fidelity CFD codes with a significantly lower computational cost.

Future work will include an in-depth analysis of the turbulence model performance for natural convection in enclosures with high Rayleigh numbers ($> 1 \times 10^{12}$) using higher-fidelity models, such as Large Eddy Simulations or Delayed Detached Eddy Simulations. Also, the effect of radiation heat transfer in natural convection heat transfer for the RCCS cavity will be assessed in more detail. In the large aspect-ratio RCCS cavity modeled, coupled radiation-convection studies showed a minimal effect of radiation on the Nusselt number along the RPV wall. However, radiation effects may become more significant when the fluid inside the RCCS cavity cannot be assumed to be transparent (e.g., a large number of suspended particles is present

in the flow) or when considering radiation reflection from the fins of the cooling standpipes. Furthermore, future studies should assess the effect of the 2D axisymmetric approximation in more detail for the range of high Rayleigh numbers, ideally using a higher-fidelity modeling approach for the flow field. Finally, results obtained using the implemented correlation in Pronghorn will be compared to CFD simulations of the RCCS to assess the accuracy of the implementation.

Acknowledgements

This manuscript has been authored by Battelle Energy Alliance, LLC under Contract No. DE-AC07-05ID14517 with the U.S. Department of Energy. The United States Government retains and the publisher, by accepting the article for publication, acknowledges that the United States Government retains a nonexclusive, paid-up, irrevocable, world-wide license to publish or reproduce the published form of this manuscript, or allow others to do so, for United States Government purposes.

This research made use of the resources of the High Performance Computing Center at Idaho National Laboratory, which is supported by the Office of Nuclear Energy of the U.S. Department of Energy and the Nuclear Science User Facilities under Contract No. DE-AC07-05ID14517.

References

[1] William R Corwin. "US Generation IV reactor integrated materials technology program". In: *Nuclear engineering and technology* 38.7 (2006), pp. 591–618.

[2] IAEA. *Design and Development of Gas Cooled Reactors with Closed Cycle Gas Turbines*. Tech. rep. IAEA-TECDOC-899. IAEA, 1996.

[3] H. Niessen and S. Ball. *Heat transport and afterheat removal for gas cooled reactors under accident conditions*. Tech. rep. IAEA-TECDOC-1163. IAEA, 2000.

[4] G. Atomics. *Gas turbine-modular helium reactor (GT-MHR) conceptual design description report*. Tech. rep. GA-910720. General Atomics, 1996.

[5] NN Ponomarev-Stepnoy et al. "Development prospects of high-temperature gas-cooled reactors and their role in nuclear power". In: *Energy* 16.1-2 (1991), pp. 119–127.

[6] Shinzo Saito, Toshiyuki Tanaka, and Yukio Sudo. *Design of high temperature engineering test reactor (HTTR)*. Tech. rep. Japan Atomic Energy Research Inst., 1994.

[7] AI Kiryushin et al. "Project of the GT-MHR high-temperature helium reactor with gas turbine". In: *Nuclear Engineering and design* 173.1-3 (1997), pp. 119–129.

[8] Z. Wu, D. Lin, and D. Zhong. "The design features of the HTR-10". In: *Nuclear Engineering and Design* 218 (2002), pp. 25–32.

[9] PM Williams et al. "MHTGR development in the United States". In: *Progress in Nuclear Energy* 28.3 (1994), pp. 265–346.

[10] Javier Ortensi et al. *NRC Multiphysics Analysis Capability Deployment FY2020-Part 3*. Tech. rep. Idaho National Lab.(INL), Idaho Falls, ID (United States), 2020.

[11] M. Methnani and B. Tyobeka. "Evaluation of high temperature gas cooled reactor performance: Benchmark analysis related to the PBMR400, PBMM, GT-MHR, HTR-10 and the astra critical facility". In: *International Atomic Energy Agency* (2013).

[12] Richard Wright. *Creep of A508/533 Pressure Vessel Steel*. Tech. rep. Idaho National Laboratory (INL), 2014.

[13] D. Lisowski et al. "Experimental studies of ngnp reactor cavity cooling system with water". In: *Proceedings of ICAPP* (2011), pp. 2–5.

[14] A. Frisani, Y. A. Hassan, and V. M. Ugaz. "Computational fluid dynamics analysis of very high temperature gas-cooled reactor cavity cooling system". In: *Nuclear Technology* 176.2 (2011), pp. 238–259.

[15] D. D. Lisowski et al. *Final Project Report on RCCS Testing with Air-based NSTF*. Tech. rep. ANL-ART-47. Argonne National Lab. (ANL), 2016.

[16] FX Trias et al. "Direct numerical simulation of a differentially heated cavity of aspect ratio 4 with Rayleigh numbers up to 1011–Part II: Heat transfer and flow dynamics". In: *International Journal of Heat and Mass Transfer* 53.4 (2010), pp. 674–683.

[17] Kevin John King. "Turbulent natural convection in rectangular air-cavities". PhD thesis. Queen Mary University of London, 1989.

[18] R Cheesewright. “Experimental Data for the Validation of Computer Codes for the Prediction of Two-Dimensional Buoyant Cavity Flows, in Significant Questions in Buoyance Affected Enclosure or Cavity Flows”. In: *ASME*. Vol. 60. 1986, pp. 75–81.

[19] A Rincón-Casado et al. “New natural convection heat transfer correlations in enclosures for building performance simulation”. In: *Engineering Applications of Computational Fluid Mechanics* 11.1 (2017), pp. 340–356.

[20] Zekeriya Altaç and Nihal Uğurlubilek. “Assessment of turbulence models in natural convection from two-and three-dimensional rectangular enclosures”. In: *International Journal of Thermal Sciences* 107 (2016), pp. 237–246.

[21] April Novak et al. “Pronghorn: A Multidimensional Coarse Mesh Application for Advanced Reactor Thermal-Hydraulics”. In: *submitted to Nucl. Techn.* ().

[22] A. Novak et al. *Pronghorn Theory Manual*. Tech. rep. INL/EXT-18-44453-Rev001. Idaho National Lab. (INL), 2020.

[23] C. Permann et al. “MOOSE: Enabling Massively Parallel Multiphysics Simulation”. In: *Preprint submitted to SoftwareX* (2020).

[24] The RELAP5 Development Team. *RELAP5/MOD3 Code Manual*. Tech. rep. NUREG/CR-5535. Idaho National Engineering Laboratory, 1995.

[25] Ray Berry et al. *RELAP-7 Theory Manual*. Tech. rep. INL/EXT-14-31366. Idaho National Laboratory, Feb. 2014.

[26] Rui Hu. *SAM Theory Manual*. Tech. rep. ANL/NE-17/4. Idaho National Engineering Laboratory, 2017.

[27] T.J. Drzewiecki et al. “The US NRC Advanced Gas REactor Evaluator (AGREE)”. In: *The 14th International Topical Meeting on Nuclear Reactor Thermalhydraulics (NURETH-14)*. 2011.

[28] Siemens. *Simcenter STAR-CCM+ User Guide V13.04*. Tech. rep. Siemens PLM, 2018.

[29] OECD/NEA. *PBMR Coupled Neutronics/Thermal-hydraulics Transient Benchmark The PBMR-400 Core Design*. Tech. rep. NEA/NSC/DOC(2013)10. OECD/NEA, July 2013.

[30] RF Warming and Richard M Beam. “Upwind second-order difference schemes and applications in aerodynamic flows”. In: *AIAA Journal* 14.9 (1976), pp. 1241–1249.

[31] William Sutherland. “LII. The viscosity of gases and molecular force”. In: *The London, Edinburgh, and Dublin Philosophical Magazine and Journal of Science* 36.223 (1893), pp. 507–531.

[32] Yaqi Wang et al. “Rattlesnake: A MOOSE-Based Multiphysics Multi-Scheme Radiation Transport Application”. In: *submitted to Nucl. Techn.* ().

[33] C Balaji and SP Venkateshan. “Interaction of surface radiation with free convection in a square cavity”. In: *International Journal of Heat and Fluid Flow* 14.3 (1993), pp. 260–267.

[34] RA Kuyper et al. “Numerical study of laminar and turbulent natural convection in an inclined square cavity”. In: *International Journal of Heat and Mass Transfer* 36.11 (1993), pp. 2899–2911.

[35] Seok-Ki Choi and Seong-O Kim. “Turbulence modeling of natural convection in enclosures: A review”. In: *Journal of Mechanical Science and Technology* 26.1 (2012), pp. 283–297.

[36] Steven L Brunton, Joshua L Proctor, and J Nathan Kutz. “Discovering governing equations from data by sparse identification of nonlinear dynamical systems”. In: *Proceedings of the national academy of sciences* 113.15 (2016), pp. 3932–3937.

[37] Bhavana Bhadriraju et al. “Operable adaptive sparse identification of systems (OASIS): application to chemical processes”. In: *AIChE Journal* (2020), e16980.

[38] Andreas Fischer and Pradyumn K Shukla. “A Levenberg–Marquardt algorithm for unconstrained multicriteria optimization”. In: *Operations Research Letters* 36.5 (2008), pp. 643–646.

[39] Alexandre Belloni, Victor Chernozhukov, and Lie Wang. “Square-root lasso: pivotal recovery of sparse signals via conic programming”. In: *Biometrika* 98.4 (2011), pp. 791–806.

[40] Paolo Balestra et al. “PBMR-400 BENCHMARK SOLUTION OF EXERCISE 1 AND 2 USING THE MOOSE BASED APPLICATIONS: MAMMOTH, PRONGHORN”. In: Mar. 2020.

Appendix A: RANS equations

This section contains the governing flow and turbulence models equations. In the RANS framework, the fields of interest, such as temperature, velocity, and pressure, in the upcoming equations represent ensemble averaged quantities.

The continuity equation in this work is:

$$\begin{aligned} \frac{\partial u_i}{\partial x_i} = 0, \quad &\text{in the Boussinesq approximation assuming small density variation} \\ \frac{\partial \rho}{\partial t} + \frac{\partial}{\partial x_i}\left(\rho u_i\right) = 0, \quad &\text{in the ideal gas approximation} \end{aligned} \tag{A.1}$$

The momentum equations are:

$$\frac{\partial \left(\rho u_i\right)}{\partial t} + \frac{\partial}{\partial x_j}\left(\rho u_i u_j\right) = -\frac{\partial p}{\partial x_i} + \frac{\partial}{\partial x_j}\left[\left(\mu + \mu_t\right)\frac{\partial u_i}{\partial x_j}\right] + \rho g_i, \tag{A.2}$$

The energy equation, solving for temperature, is

$$\frac{\partial \left(\rho c_p T\right)}{\partial t} + \frac{\partial}{\partial x_i}\left(\rho c_p u_i T\right) = +\frac{\partial}{\partial x_i}\left[\left(k + k_t\right)\frac{\partial T}{\partial x_i}\right], \tag{A.3}$$

Eqs. A.2 and A.3 still need closure, as the density ρ, the turbulent viscosity μ_t and the turbulent thermal conductivity k_t require a model.

The density ρ in Eq. A.2 is modeled as

$$\begin{aligned} \rho = \rho_0\left[1 - \beta\left(T - T_0\right)\right], \quad &\text{in the Boussinesq approximation} \\ \rho = \frac{P_{ref}}{RT}, \quad &\text{in the ideal gas approximation} \end{aligned} \tag{A.4}$$

In the following subsection, the modeling of the turbulent viscosity for the $k-\omega\ SST-\gamma$ model is presented using reference [28].

A.1 $k-\omega\ SST-\gamma$

To determine the turbulent viscosity, the KWSST Gamma solves extra equations for the turbulent kinetic energy k, the specific turbulent dissipation rate ω, and the intermittency parameter γ.

The turbulent eddy viscosity μ_t in this model is:

$$\mu_t = \rho k\ min(\frac{\alpha^*}{\omega}, \frac{a_1}{S\,F_2}), \tag{A.5}$$

where α^* and a_1 are model coefficients and S is the mean strain rate tensor. F_2 is a blending function calculated as:

$$F_2 = tanh\left(\left(max\left(\frac{2\sqrt{k}}{\beta^*\omega d}, \frac{500\nu}{d^2\omega}\right)\right)^2\right) \tag{A.6}$$

where β^* is a model coefficient and d is the distance to the wall.

The transport equations solved are:

$$\begin{aligned}
\frac{\partial(\rho k)}{\partial t}+\frac{\partial}{\partial x_i}(\rho u_i k)&=\frac{\partial}{\partial x_i}\left[(\mu+\mu_t\sigma_k)\frac{\partial k}{\partial x_i}\right]+P_k-\gamma'\rho\beta^* f_{\beta^*}(\omega k),\\
\frac{\partial(\rho\omega)}{\partial t}+\frac{\partial}{\partial x_i}(\rho u_i \omega)&=\frac{\partial}{\partial x_i}\left[(\mu+\mu_t\sigma_\omega)\frac{\partial \omega}{\partial x_i}\right]+P_\omega-\rho\beta f_(\omega^2),\\
\frac{\partial(\rho\gamma)}{\partial t}+\frac{\partial}{\partial x_i}(\rho u_i \gamma)&=\frac{\partial}{\partial x_i}\left[\left(\mu+\frac{\mu_t}{\sigma_f}\right)\frac{\partial \gamma}{\partial x_i}\right]+P_\gamma-E_\gamma,
\end{aligned} \tag{A.7}$$

where:

$$\begin{aligned}
P_k&=\gamma(G_k+G_b)+{G_k}^{lim},\\
P_\omega&=(G_\omega+D_\omega),\\
P_\gamma&=100\rho S\gamma(1-\gamma)F_{onset},\\
F_{onset}&=max(F_{onset2}-F_{onset3},0),\\
F_{onset2}&=min(F_{onset1},2),\\
F_{onset3}&=max\left[1-(Re_t/3.5)^3,0\right],\\
F_{onset1}&=\frac{Re_v}{C_{onset1}Re_{\theta c}},\\
\\
E_\gamma&=C_{a2}\rho W\gamma F_{turb}(C_{e2}\gamma-1),\\
F_{turb}&=exp\left[-(Re_t/2)^2\right],\\
\\
G_k&=\mu_t S^2-\frac{2}{3}\rho k\frac{\partial u_i}{\partial x_i}-\frac{2}{3}\mu_t\left(\frac{\partial u_i}{\partial x_i}\right)^2,\\
G_b&=\beta\frac{\mu_t}{Pr_t}(\frac{\partial T}{\partial x_i}g_i),\\
{G_k}^{lim}&=5\,max(\gamma-0.2,0)(1-\gamma){F_{on}}^{lim}\,max(3\mu-\mu_t,0)SW,\\
{F_{on}}^{lim}&=min\left(max\left(\frac{Re_v}{2.2\dot{1}000},0\right),3\right),\\
G_\omega&=\rho\gamma\left[\left(S^2-\frac{2}{3}\frac{\partial {u_i}^2}{\partial x_i}\right)-\frac{2}{3}\omega\frac{\partial u_i}{\partial x_i}\right],\\
D_\omega&=2\rho(1-F_1)\sigma_{\omega_2}\frac{1}{\omega}\frac{\partial k}{\partial x_i}\frac{\partial \omega}{\partial x_i},\\
F_1&=tanh\left(\left[min\left(max\left(\frac{\sqrt{k}}{0.09\omega d},\frac{500\nu}{d^2\omega}\right),\frac{2k}{d^2CD_{k\omega}}\right)\right]^4\right),\\
\gamma'&=min\left[max(\gamma,0.1)\,1\right],
\end{aligned} \tag{A.8}$$

In the above presented equations, β, σ_k, σ_ω, $\sigma_{\omega 2}$, σ_f, C_{onset1}, C_{a2}, and C_{e2} are model coefficients. f_{beta^*} is a dissipation limiter to enhance the modeling of free-shear flows. S and W are the moduli of the strain rate tensor and rotation rate tensor, respectively. $Re_{\theta c}$ is known as the critical Reynolds number, and it is calculated via a correlation rather than being solved for.

Generally speaking, the intermittency parameter γ represents the percentage of time that turbulent fluctuations are present in the boundary layer. It is particularly useful in flows that undergo transition, i.e., flows whose boundary layers have a significant laminar contribution. As seen in Eq. A.7, the turbulent kinetic energy production term is multiplied by γ. This parameter takes values between 0 and 1, which means that it damps the turbulent kinetic energy production term such that it is 0 in a laminar boundary layer and 1 in a turbulent boundary layer. In addition, the model also adjusts the dissipation of the turbulent kinetic energy according to the value of γ, ensuring that the dissipation does not drop below 10% of the turbulent value.

Analyzing the equation for the intermittency parameter γ, we notice that F_{onset} acts as a switch to the production of intermittency. This parameter is a function of the critical Reynolds number $Re_{\theta c}$, which is defined using the momentum thickness in a boundary layer as its characteristic length. Thus, at a specific value of momentum thickness, the transition to turbulence will occur. The critical Reynolds number is found via a correlation, which works well for flat geometries in general. The correlation used is:

$$Re_{\theta c} = C_{TU1} + C_{TU2} exp\left[-C_{TU3} T_{uL} F_{PG} \lambda_{\theta L}\right], \tag{A.9}$$

where C_{TU1}, C_{TU2} and C_{TU3} are model coefficients, $T_{uL} = min\left(100\frac{\sqrt{2k/3}}{\omega d}, 100\right)$, and

$\lambda_{thetaL} = min\left[max\left(-7.57 \cdot 10^{-3}\frac{d^2}{v}\nabla(n\cdot\overline{u})\cdot n + 0.0128, -1\right), 1\right]$

Appendix B: Details of the PLOFC transient simulation with Rattlesnake and Pronghorn

Realistic nonisothermal temperature profiles at the RPV wall in the operational regime of the RCCS can be obtained by analyzing accident scenarios. Since measurements from full scale experiments are not available, international benchmarks on PBRs are the next best sources of information. The multiphysics PBMR-400 transient benchmark [29] is the most successful and comprehensive benchmark on accident simulation for PBRs. The results for the PLOFC exercise in the PBMR-400 benchmark provide a realistic RPV wall temperature profile evolution(i.e., accepted by the PBRs designer community) . The temperature profiles obtained in this section assist our purposes of studying the dependency of the Nusselt number on the non-isothermal boundary conditions.

The benchmark design has been derived from the PBMR-400 demonstration power plant[29]. The PBMR-400 is a modular thermal reactor moderated with graphite and cooled with helium. The 9.6% enriched uranium dioxide fuel is encapsulated by different shells of pyrolytic graphite and ceramic material and is called a TRISO (Tristructural isotropic) particle. Almost 15,000 TRISO particles are contained in every one of the almost 452,000 pebbles. The pebbles are contained in an annular region, they enter the core at the top and leave it through the defueling chute at the bottom. At the bottom outlet, pebbles are either recirculated or discarded, based on their burnup; a pebble makes an average of six passes through the core. During normal operation, 192.7 kg/s of helium at an inlet temperature of 773 K flow through the pebbles from the top to the bottom reaching roughly 1173 K at the outlet.

Several simplifications have been applied to the benchmark problem geometry to reduce the number of approximations that every participant have to introduce in their models due to the different codes' capabili-

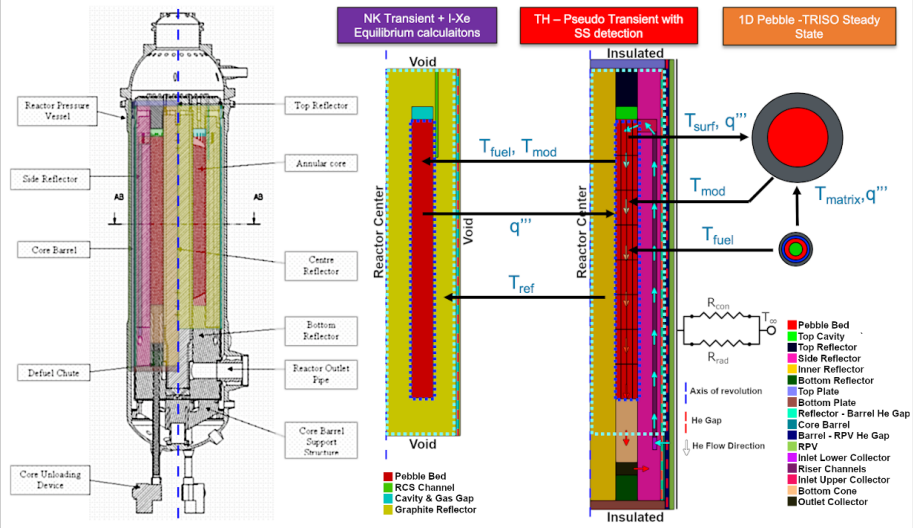

Figure 17: PBMR-400 Models and coupling scheme.

ties. A prime example is the inlet of the helium into the pebble bed. Helium usually enters the upper plenum well above the pebble bed, but, due to shortcomings in the geometry representation in some legacy codes, helium enters just below the top of the pebble bed. In addition, the central reflector is not cooled in the benchmark model while the actual PBMR-400 design has an engineered coolant flow through the central reflector.

The PBMR-400 geometry, the Pronghorn/Rattlesnake coupled model, and the coupling scheme are depicted in Fig. 17. The Rattlesnake and Pronghorn model use axisymmetric geometry to model the PBMR-400 geometry. The neutronics model comprises two energy groups and 115 material regions: 110 for the pebble bed (red), one for the reflector (yellow), one for the control rod (green), and two for the two void areas (cyan); the neutronics model does not include the neutronically unimportant region at the periphery of the core. The thermal-hydraulics model includes a larger fraction of the reactor compared to the neutronics model. The arrows indicate the flow path. Helium traverses different porous components, including the inlet lower collector, the outlet collector (20% porosity), and the pebble bed (39% porosity). The fluid flow domain is limited to just these components, while the solid conduction equations are solved on the whole domain depicted in Fig. 17 to take into account the heat conducted from the core to the outside boundary through the reflector, the barrel, and reactor pressure vessel (RPV). Radiation across the reflector/barrel and RCCS gap are accounted for by MOOSE's gap heat transfer module; in this module, radiative heat transfer is simplified to only occur between the nearest nodes of the left and right surfaces. The top, bottom, center, and centerline of the axysimmetric model are considered adiabatic, where the normal heat flux is set to zero. On the right boundary, a thermal resistance model, taking into account the radiation, the conduction through, and the stagnant (benchmark assumption) air gap between the RPV and the reactor cavity cooling system (RCCS) at 293.15 K, has been imposed. A more detailed discussion of the Rattlesnake/Pronghorn model can be found in Ref. [40].

The PLOFC transient is initiated from steady-state conditions that are computed using a coupled neutron kinetics/thermal-hydraulics multiphysics simulation. In this simulation, Rattlesnake solves a k-eigenvalue problem while Pronghorn computes the corresponding temperature profile. The two codes are coupled via

the power distribution computed by Rattlesnake and the temperature distribution computed by Pronghorn. From the steady-state conditions, the inlet mass flow rate and the outlet pressure are linearly ramped to 0 kg/s and 60 bar over a period of thirteen seconds. After the first thirteen seconds, all the control rods are inserted with constant velocity within three seconds, immediately reducing the prompt power to zero; only the decay heat is active throughout the transient so that the transient itself does not require a neutron kinetics solution anymore. Starting from the time of the SCRAM, the core helium inventory remains constant, and natural circulation sets in. The transient is completed fifty hours after the SCRAM.